

# Effectors Enabling Adaptation to Mitochondrial Complex I Loss in Hürthle Cell Carcinoma



Raj K. Gopal<sup>1,2,3,4,5</sup>, Venkata R. Vantaku<sup>5,6</sup>, Apekshya Panda<sup>1,2</sup>, Bryn Reimer<sup>1,2</sup>, Sneha Rath<sup>1,2</sup>, Tsz-Leung To<sup>1,2</sup>, Adam S. Fisch<sup>7</sup>, Murat Cetinbas<sup>1,5</sup>, Maia Livneh<sup>7</sup>, Michael J. Calcaterra<sup>6</sup>, Benjamin J. Gigliotti<sup>8</sup>, Kerry A. Pierce<sup>2</sup>, Clary B. Clish<sup>2</sup>, Dora Dias-Santagata<sup>5,7</sup>, Peter M. Sadow<sup>4,5,7</sup>, Lori J. Wirth<sup>3,4,5</sup>, Gilbert H. Daniels<sup>3,4,5,9</sup>, Ruslan I. Sadreyev<sup>1,5,7</sup>, Sarah E. Calvo<sup>1,2</sup>, Sareh Parangi<sup>4,5,6</sup>, and Vamsi K. Mootha<sup>1,2,3,10</sup>

Downloaded from <https://aacr.journals.org/cancerdiscovery> on 13/08/19. DOI: 10.1158/1538-7445.2019.013104

by guest on 15 May 2026

**ABSTRACT**

Oncocytic (Hürthle cell) carcinoma of the thyroid (HCC) is genetically characterized by complex I mitochondrial DNA mutations and widespread chromosomal losses. Here, we utilize RNA sequencing and metabolomics to identify candidate molecular effectors activated by these genetic drivers. We find glutathione biosynthesis, amino acid metabolism, mitochondrial unfolded protein response, and lipid peroxide scavenging to be increased in HCC. A CRISPR–Cas9 knockout screen in a new HCC model reveals which pathways are key for fitness, and highlights loss of GPX4, a defense against lipid peroxides and ferroptosis, as a strong liability. Rescuing complex I redox activity with the yeast NADH dehydrogenase (ND11) in HCC cells diminishes ferroptosis sensitivity, while inhibiting complex I in normal thyroid cells augments ferroptosis induction. Our work demonstrates unmitigated lipid peroxide stress to be an HCC vulnerability that is mechanistically coupled to the genetic loss of mitochondrial complex I activity.

**SIGNIFICANCE:** HCC harbors abundant mitochondria, mitochondrial DNA mutations, and chromosomal losses. Using a CRISPR–Cas9 screen inspired by transcriptomic and metabolomic profiling, we identify molecular effectors essential for cell fitness. We uncover lipid peroxide stress as a vulnerability coupled to mitochondrial complex I loss in HCC.

See related article by Frank et al., p. 1884.

**INTRODUCTION**

Oncocytic (Hürthle cell) carcinoma of the thyroid (HCC) has a tendency for aggressive behavior and an intrinsic resistance to radioactive iodine (RAI), a central therapy for patients with well-differentiated thyroid cancer (1). HCC is a unique subtype of differentiated thyroid cancer in that it has a notable abundance of dysmorphic mitochondria, a histologic morphology seen in oncocytic neoplasms (2). Although oncocytic tumors of other anatomic sites, such as renal oncocytoma (RO), are predominantly indolent, HCC can have distant metastases with strong uptake of fluorodeoxyglucose on PET imaging (3).

The genetic underpinnings of HCC include complex I mitochondrial DNA (mtDNA) mutations and widespread chromosomal losses. Although early targeted studies identified

mtDNA mutations and marked aneuploidy as characteristic of HCC (4–8), the role of these events was difficult to contextualize in the absence of a comprehensive genetic analysis. Two recent whole-exome HCC studies established that mtDNA mutations and widespread chromosomal losses are the defining driver events in HCC (9, 10). The mtDNA mutations are disruptive and significantly enriched in complex I genes, suggesting loss of the first step in mitochondrial oxidative phosphorylation (OXPHOS) similar to other oncocytic tumors (11–13). In the nuclear genome, chromosomal loss events result in extensive loss of heterozygosity (LOH), culminating in either a near-haploid or uniparental disomic state. A detailed phylogenetic analysis revealed that widespread LOH and mtDNA complex I mutations are truncal events maintained during tumor evolution, further supporting their role in tumor initiation and progression (9).

The core molecular effectors activated in the face of the mitochondrial and nuclear genomic alterations of HCC have not been well characterized. Efforts to uncover these molecular pathways and move toward implementing novel therapeutic strategies have stalled due to an absence of reliable HCC models. Existing gene expression and metabolic analyses of HCC have identified changes in the tricarboxylic acid cycle as well as activation of the mTOR pathway (14–17). The growth-promoting and adaptive pathways activated by loss of mitochondrial complex I, however, have not been well characterized in HCC.

To address these questions, we performed joint RNA sequencing (RNA-seq) and metabolomic profiling of an HCC cohort with matched normal thyroid samples and found coordinated upregulation in amino acid and glutathione biosynthesis, as well as the accumulation of lipids with polyunsaturated fatty acids (PUFA) in tumors. A CRISPR–Cas9 screen together with targeted drug screening validates the essentiality of these metabolic pathways in newly created authentic HCC disease models. We further identify lipid peroxide stress as a novel vulnerability that is mechanistically coupled to mitochondrial complex I loss and that can potentially be exploited to treat patients with HCC.

<sup>1</sup>Howard Hughes Medical Institute and Department of Molecular Biology, Massachusetts General Hospital, Boston, Massachusetts. <sup>2</sup>Broad Institute of MIT and Harvard, Cambridge, Massachusetts. <sup>3</sup>Department of Medicine, Massachusetts General Hospital, Boston, Massachusetts. <sup>4</sup>Cancer Center, Massachusetts General Hospital, Boston, Massachusetts. <sup>5</sup>Harvard Medical School, Boston, Massachusetts. <sup>6</sup>Department of Surgery, Massachusetts General Hospital, Boston, Massachusetts. <sup>7</sup>Department of Pathology, Massachusetts General Hospital, Boston, Massachusetts. <sup>8</sup>Department of Medicine, University of Rochester, Rochester, New York. <sup>9</sup>Thyroid Unit, Massachusetts General Hospital, Boston, Massachusetts. <sup>10</sup>Department of Systems Biology, Harvard Medical School, Boston, Massachusetts.

**Note:** R.K. Gopal and V.R. Vantaku contributed equally to this article.

**Corresponding Authors:** Vamsi K. Mootha, Molecular Biology, Massachusetts General Hospital, 185 Cambridge Street, 6th Floor, Boston, MA 02114. Phone: 617-643-3059; E-mail: vamsi\_mootha@hms.harvard.edu; and Sareh Parangi, 15 Parkman Street, WAC 460, Boston, MA 02114. Phone: 617-831-7798; Fax: 617-243-6853; E-mail: sparangi@mgh.harvard.edu  
Cancer Discov 2023;13:1904–21

doi: 10.1158/2159-8290.CD-22-0976

This open access article is distributed under the Creative Commons Attribution 4.0 International (CC BY 4.0) license.

©2023 The Authors; Published by the American Association for Cancer Research

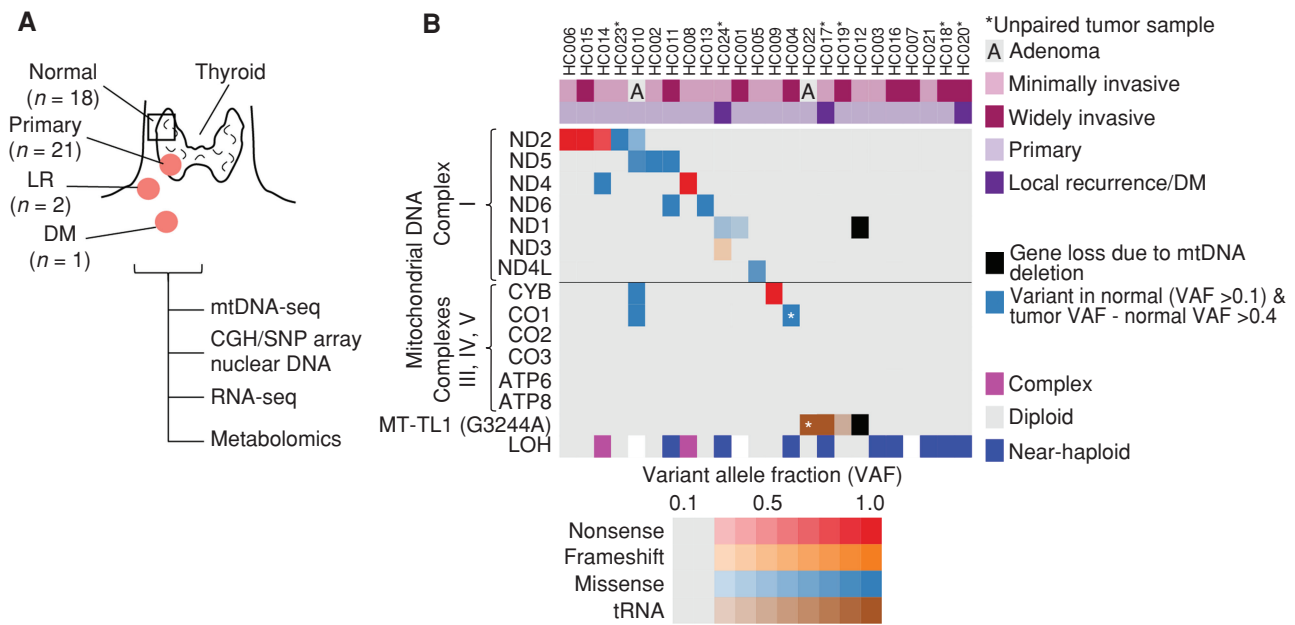


**Figure 1.** An HCC cohort with complex I mtDNA mutations and chromosomal losses. **A**, Clinical cohort of HCC and normal thyroid samples with profiling methods used. CGH, comparative genomic hybridization; primary, primary tumor. **B**, Mutations in mtDNA organized by complex with allelic fraction  $>0.2$  with CGH-SNP array copy-number profile. See also Supplementary Fig. S1.

## RESULTS

### An HCC Cohort with Complex I mtDNA Mutations and Chromosomal Losses

With the goal of performing RNA-seq and metabolomic profiling, we established a new cohort of fresh-frozen HCC samples and confirmed their mtDNA mutation status and chromosomal copy number. This cohort, which was almost entirely distinct from our recent whole-exome analysis (9), contained 24 oncocyctic (Hürthle cell) tumors, with 18 cases having matched normal thyroid tissue (Supplementary Table S1). Tumor samples included 21 primary tumors comprised of 19 HCC (eight widely invasive, 11 minimally invasive) and two oncocyctic (Hürthle cell) adenomas, as well as two locoregional recurrences (LR) and one distant metastasis (DM; Fig. 1A).

Next-generation mtDNA sequencing identified 18 of the 24 tumors (75%) to harbor an mtDNA alteration at  $>0.20$  variant allele fraction (VAF), a surrogate of heteroplasmy (Fig. 1B; Supplementary Table S2). There were 14 tumors with disruptive mtDNA mutations in OXPHOS encoding genes, including 12 complex I, one complex III, and one complex IV mutant tumors (Fig. 1B). Three tumors contained a tRNA variant in *MT-TL1* (G3244A) previously associated (18) with mitochondrial encephalomyopathy, lactic acidosis, and stroke-like episodes (MELAS), a mitochondrial disorder associated with complex I deficiency (Fig. 1B). Finally, one tumor contained a 3,710 bp deletion that led to the loss of a complex I gene (*MT-ND1*) and *MT-TL1* (Fig. 1B; Supplementary Fig. S1A). We confirmed these mtDNA alterations in 16 of 18 samples using RNA-seq and found concordant variant calls in three patients who were part of our prior exome cohort (Supplementary Table S2).

We used array-based comparative genomic hybridization CGH (aCGH) combined with SNP microarrays to determine

the nuclear DNA copy-number state in our sample cohort. The chromosomal state was identified in 21 of 24 samples, with the remaining three samples not passing quality control. Tumors existed in three copy-number profiles: “diploid” ( $n = 10$ ), “near-haploid” ( $n = 9$ ), and “complex” ( $n = 2$ ; Fig. 1B; Supplementary Fig. S1B; Supplementary Table S2). All 10 diploid tumors harbored a disruptive OXPHOS alteration. In addition, of the six tumors with no mtDNA changes, the five with reliable aCGH and SNP array data were all near-haploid (Fig. 1B).

Overall, our new cohort of patients with HCC, which we established for RNA-seq and metabolomic profiling, recapitulates the key nuclear DNA and mtDNA findings that are predicted based on recent exome analyses of HCC (9, 10).

### Transcriptional Landscape of HCC

We performed bulk RNA-seq on our entire cohort to identify differentially expressed molecular programs in HCC. Principal component analysis (PCA) showed all tumors, regardless of mtDNA or chromosomal status, clustered along the first principal component (PC1; 22.5% of the variance; Fig. 2A). The four samples diverging along the second principal component (PC2) had Hashimoto thyroiditis with PC2 loadings comprised of immunoglobulin genes (Fig. 2A; Supplementary Table S3). We observed significant differences in gene expression with 1,987 upregulated and 4,337 downregulated transcripts (adjusted  $P < 0.001$ ; Supplementary Table S3).

We first focused our analysis on known clinical and histologic features of HCC, including its increased  $^{18}$ fluorodeoxyglucose uptake on PET imaging, its decreased uptake of RAI, and its accumulation of mitochondria (Fig. 2B; refs. 2, 3, 19). Glycolysis genes, including the redox-dependent GAPDH step, showed consistent upregulation in HCC, whereas TXNIP, a key negative regulator of glucose uptake with a tumor suppressor function,

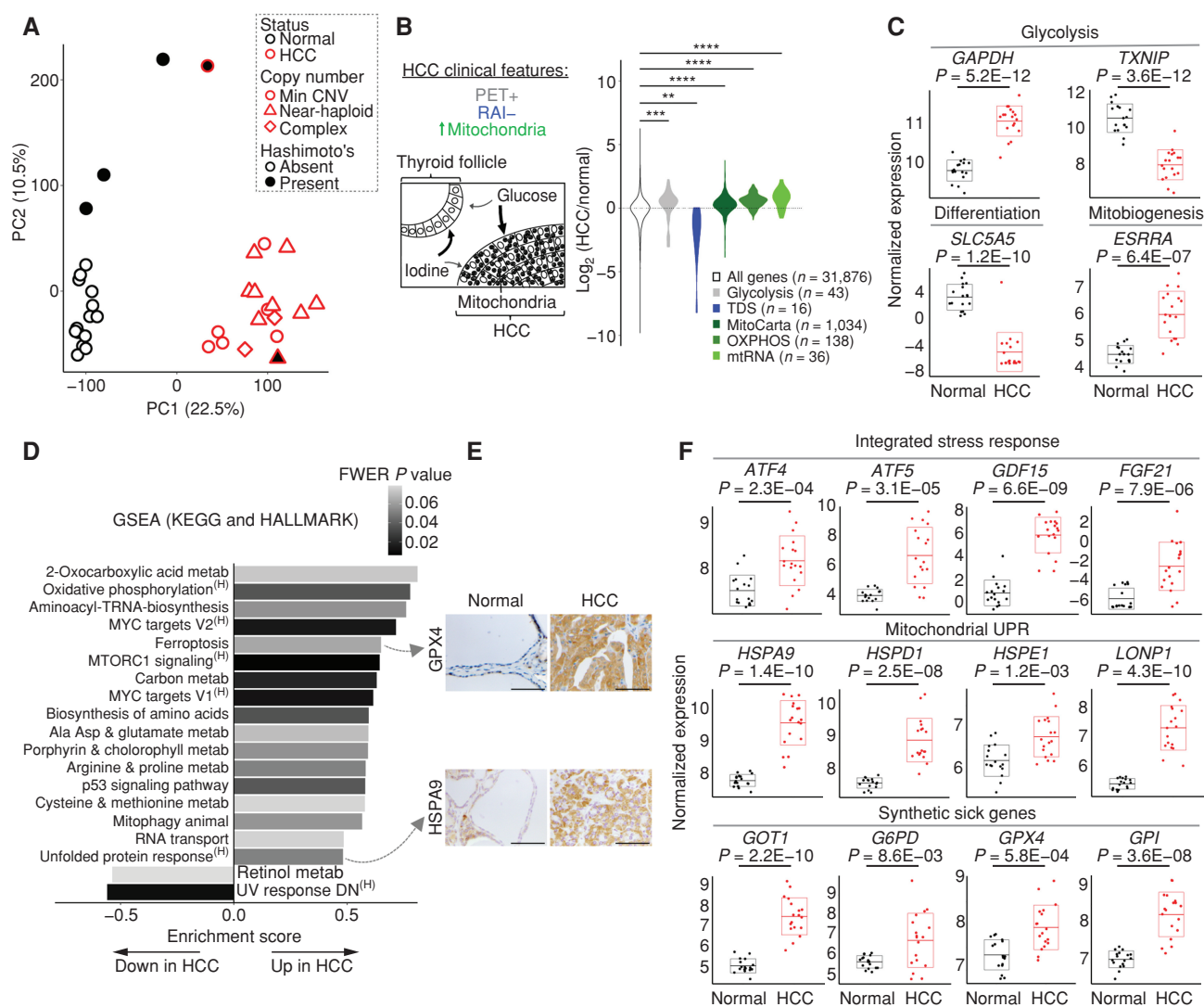


**Figure 2.** Transcriptomic landscape of HCC. **A**, PCA of HCC and normal thyroid ( $n = 18$  each) RNA-seq. Hashimoto's, Hashimoto thyroiditis; Min CNV, minimum copy-number variation. **B**, Schematic of HCC clinical features with violin plots of gene expression fold changes (HCC/normal) for related molecular pathways. mtRNA, mitochondrial RNA; TDS, thyroid differentiation score. Significance tested by the Kolmogorov-Smirnov test: \*\*,  $P < 1.0E-03$ ; \*\*\*,  $P < 1.0E-04$ ; \*\*\*\*,  $P < 1.0E-05$ . **C**, Normalized gene expression for transcripts with adjusted  $P$  values. **D**, Gene set enrichment analysis (GSEA) of the KEGG and HALLMARK pathways ranked by enrichment score with shaded FWER values. <sup>(H)</sup>, HALLMARK gene set; metab, metabolism. **E**, IHC for proteins from selected pathways in HCC and normal thyroid; scale bars, 200  $\mu$ m. **F**, Normalized gene expression for transcripts from selected pathways with adjusted  $P$  values. "Synthetic sick genes" refers to knockouts that were synthetic sick with OXPPOS dysfunction (35). Horizontal lines show the mean, and boxes show the standard deviation. See also Supplementary Fig. S2.

showed striking downregulation (Fig. 2B and C; refs. 20, 21). In line with the resistance of HCC to RAI, we observed clear downregulation in the 16 genes relevant to iodine metabolism that comprise the thyroid differentiation score (TDS), including dramatic downregulation of the sodium-iodide symporter, *SLC5A5* (Fig. 2B and C; ref. 22). We found mitochondrial transcripts, defined by the MitoCarta3.0 inventory (23), to be consistently increased in HCC, including OXPPOS and mitochondrial RNA (mtRNA) genes (Fig. 2B). Furthermore, we confirmed significant upregulation of *ESRRA* (Fig. 2C), a key transcription factor involved in mitochondrial biogenesis (24), as has been reported previously in this tumor (25).

To uncover novel transcriptional pathways present in HCC, we performed gene set enrichment analysis (26, 27) on the HCC

transcriptome (Supplementary Table S3). We focused on gene sets from the HALLMARK and Kyoto Encyclopedia of Genes and Genomes (KEGG) databases that were significantly altered in HCC [family-wise error rate (FWER)  $P \leq 0.08$ ]. We identified 18 gene sets to be significantly enriched and two gene sets to be significantly repressed in HCC (Fig. 2D). Among enriched pathways, we found activation of classic oncogenic signaling (mTOR and MYC) and numerous pathways related to amino acid metabolism. We also found stress response programs, such as ferroptosis (an iron-dependent form of regulated cell death), mitophagy, and the unfolded protein response (UPR) to be activated in HCC (Fig. 2D). Closer inspection of the UPR gene set suggested preferential activation of the mitochondrial UPR (28, 29) in HCC, which we confirmed through a survey

of all heat shock protein family members (Supplementary Fig. S2A). Furthermore, gene set enrichment analysis (GSEA) on MitoCarta3.0 genes identified “protein homeostasis” as the most significantly enriched mitochondrial pathway in HCC (Supplementary Fig. S2B).

We sought to validate the enrichment of select programs in HCC using IHC. Increased immunoreactivity of GPX4 (a selenoprotein that protects against ferroptosis by scavenging lipid hydroperoxides) and HSPA9 (a member of the mitochondrial UPR) in HCC cells corroborated the transcriptional enrichment for the ferroptosis and UPR pathways (Fig. 2E, top and bottom). However, IHC for phospho-S6 (Ser235/236), a marker of mTOR activation, showed more pronounced staining in stroma and blood vessels compared with HCC cells despite strong total S6 staining throughout (Supplementary Fig. S2C). This staining pattern suggests that full engagement of the mTOR response may preferentially occur in the tumor microenvironment.

The enrichment of the UPR, along with pathways related to amino acid metabolism, suggested that the integrated stress response (ISR) was activated in HCC (30). ISR transcripts were significantly increased in HCC, including *ATF4* and *ATF5* (key transcription factors coordinating the ISR), as well as *GDF15* and *FGF21* (cytokines associated with the ISR; Fig. 2F, top; refs. 31, 32). Moreover, as the mitochondrial UPR has been associated with ISR activation, a focused look at key mitochondrial UPR members, including *HSPA9*, *HSPD1*, *HSPE1*, and *LONP1*, confirmed coordinated upregulation of this pathway in HCC (Fig. 2F, middle; refs. 33, 34).

To identify pathways that promote the survival of HCC in the face of complex I loss, we considered the expression of genes previously identified from a genome-wide CRISPR-Cas9 knockout screen to cause synthetic sickness with mitochondrial dysfunction (35). We predicted that the expression of such “predefined synthetic sick genes” would be defended or upregulated in HCC due to mitochondrial dysfunction caused by mtDNA mutations. Consistent with our prediction, nearly all of the 14 predefined synthetic sick genes present in our RNA-seq data were upregulated, and nine of these genes were part of enriched gene sets in HCC (Supplementary Fig. S2D). It was notable that genes involved in glycolysis (*GPI*), amino acid metabolism (*GOT1*), the pentose phosphate pathway (*G6PD*), and lipid peroxide detoxification (*GPX4*) were represented as potential metabolic vulnerabilities whose expression was increased (Fig. 2F, bottom).

### Metabolic Landscape of HCC

In parallel, we investigated the HCC metabolome using four liquid chromatography–tandem mass spectrometry (LC-MS) methods that jointly quantified 617 known metabolites (Supplementary Table S4). The metabolome of HCC was distinct from normal thyroid, with 440 known metabolites found to be differentially abundant (adjusted  $P < 0.01$ ), and

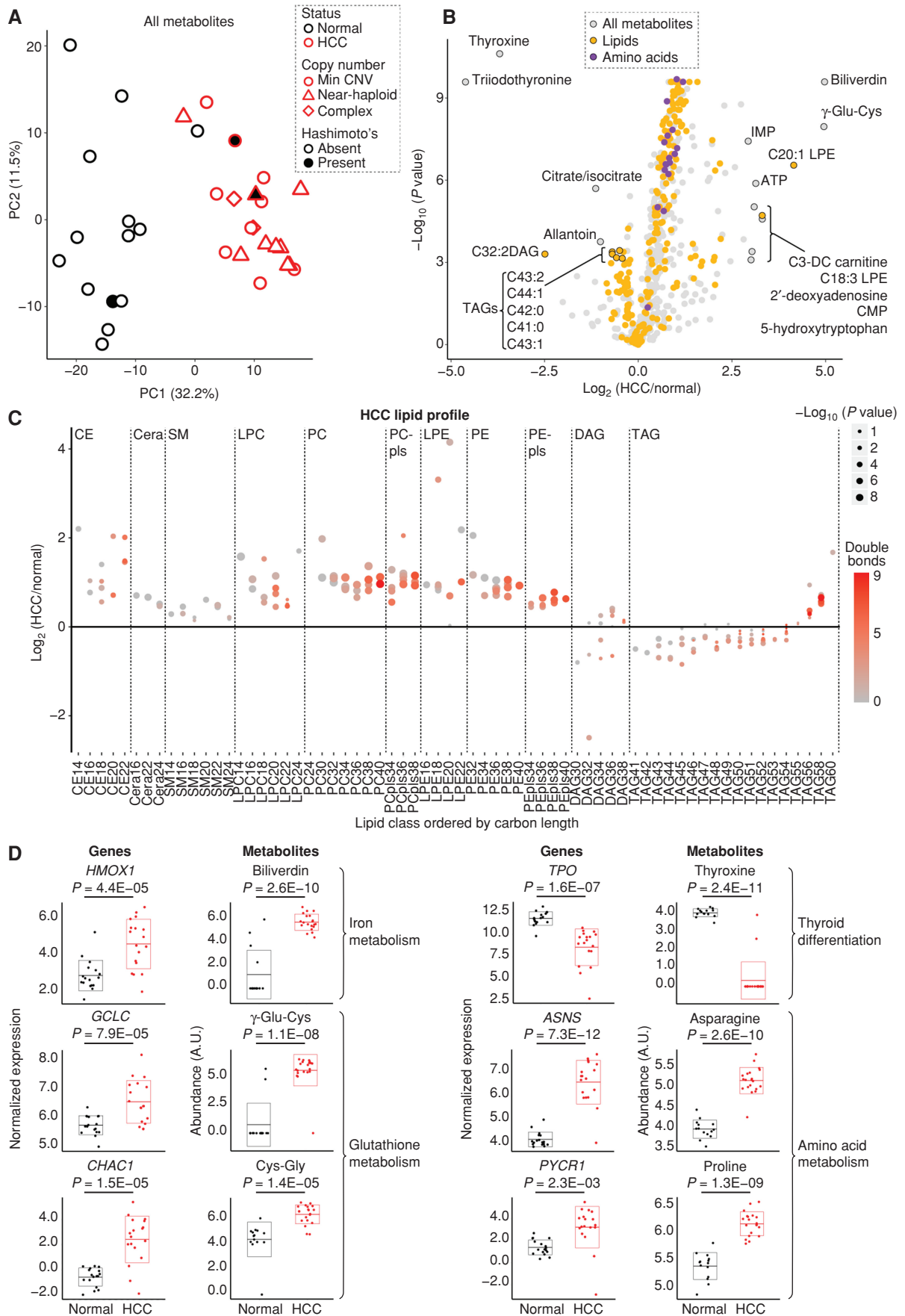
PCA analysis of all known metabolites showed tumors to be distinct from normal along PC1 (32.2% of the variance; Fig. 3A; Supplementary Table S4). Among the most significantly changing metabolites in HCC, we found those related to thyroid differentiation (thyroxine and triiodothyronine) to be decreased, whereas those related to glutathione [ $\gamma$ -glutamyl-cysteine ( $\gamma$ -Glu-Cys)] and heme (biliverdin) were increased (Fig. 3B). Consistent with the strong transcriptional changes in amino acid metabolism, we observed amino acids to be enriched in upgoing HCC metabolites (Fig. 3B).

A more detailed analysis of lipids in HCC revealed a differential abundance of specific categories of lipid species, including an accumulation of PUFAs. In contrast to multiple triacylglycerols (TAG) that were decreased, lysophosphatidylethanolamine (LPE) species were increased in HCC (Fig. 3B). Closer inspection of lipid classes showed preferential increases in ether and glycerophospholipids, as well as sterol and prenol species (Supplementary Fig. S3A). When the lipids were plotted as a function of carbon and double bond number, we found similar increases in saturated, monounsaturated, and polyunsaturated levels of cholesterol ester (CE), and glycerophospholipid species (Fig. 3C; Supplementary Fig. S3B). On the other hand, we discovered a preferential increase of TAGs with more total carbons in HCC (Fig. 3C). The elevated levels of phosphatidylethanolamines with PUFA side chains along with increased adrenate and arachidonate suggest that lipid substrates capable of ferroptosis accumulate in HCC (Fig. 3C; Supplementary Fig. S3C; refs. 36, 37).

### Concordance of Transcriptional and Metabolomic Profiles

The most differentially abundant metabolites in HCC directly connected to key transcriptional changes revealed in our RNA-seq data. The two most decreased metabolites, thyroxine and triiodothyronine, corroborate the transcriptional evidence for a nonthyrocyte state with decreased thyroid hormone production in HCC (Fig. 3D). The top two increased metabolites, biliverdin and  $\gamma$ -Glu-Cys, are products of two transcriptionally upregulated reactions, *HMOX1* and *GCLC*, respectively, that were leading-edge genes in the ferroptosis gene set (Fig. 3D). We also found significant upregulation of the  $\gamma$ -glutamylcyclotransferase *CHAC1*, a ferroptosis biomarker, as well as its product cysteinyl-glycine (Cys-Gly), suggesting a potential state of cysteine stress in HCC (Fig. 3C; ref. 38). A closer look at glutathione metabolism revealed increased levels of reduced and oxidized glutathione, homocysteine, and cystathionine along with transcriptional changes that suggested activation of the  $\gamma$ -glutamyl cycle and stalling of transsulfuration in HCC (Supplementary Fig. S3D and S3E). Finally, the three most significantly increased amino acids were alanine, asparagine, and proline, which are products of reactions identified by our GSEA to be significantly upregulated, including the

**Figure 3.** Metabolic signatures of HCC. **A**, PCA of metabolomics from four mass spectrometry methods in HCC ( $n = 20$ ) and normal thyroid ( $n = 14$ ). Hashimoto's, Hashimoto thyroiditis; Min CNV, minimum copy-number variation. **B**, Volcano plot showing fold change (HCC/normal; x-axis) and adjusted  $P$  value (y-axis), with metabolites annotated by name and color. CMP, cytidine monophosphate; IMP, inosine monophosphate. **C**, Differential abundance of lipids organized by class and sorted by the number of carbons with double bonds (color) and adjusted  $P$  values (dot size). Cera, ceramide; DAG, diacylglycerol; LPC, lysoPC; PC, phosphatidylcholine; PE, phosphatidylethanolamine; pls, plasmalogen; SM, sphingomyelin. **D**, Normalized expression and abundance for enzymes and their metabolic products, respectively, with adjusted  $P$  values. Horizontal lines show the mean, and boxes show the standard deviation. See also Supplementary Fig. S3.



Downloaded from <http://aacrjournals.org/cancerdiscovery/article-pdf/13/8/1904/3353133/1904.pdf> by guest on 15 May 2026

ASNS and *PYCR1* genes (Fig. 3D). Collectively, our joint transcriptomic and metabolomic profiling highlights changes in glutathione, amino acid, and lipid metabolism in HCC.

### Establishing Authentic HCC Models

Given that the field of HCC biology has been hampered by a lack of experimental models, we sought to create patient-derived cell lines to overcome this barrier. We successfully generated a patient-derived HCC cell line using tailored culture conditions from patient HC024 (hereafter referred to as “MGH-HCC1”). We also obtained a separate HCC patient-derived xenograft (PDX) sample from the NCI Patient-Derived Models Repository from which we generated mouse xenografts and an additional cell line (<https://pdmr.cancer.gov>; distribution lot name 248138-237-R; hereafter referred to as “NCI-HCC”).

To credential MGH-HCC1 and NCI-HCC cells as authentic cellular models of HCC, we compared the mtDNA and chromosomal copy-number status of each cell line with an immortalized normal thyroid cell line (Nthy-ori 3-1). Sequencing of the mtDNA identified the following: (i) a disruptive complex I mutation in MGH-HCC1 (*MT-ND1*: m.G3745A, 60.2% heteroplasmy; the same mutation identified by our original sequencing of the patient’s tumor); (ii) disruptive homoplasmic mutations in two complex I genes in NCI-HCC (*MT-ND1*: m.G3916A, 99.8%; *MT-ND5*: m.CA12417C, 99.9%); and (iii) no alterations in Nthy-ori 3-1 cells (Figs. 1B and 4A; Supplementary Table S2). Both HCC cell lines were thereby established to be complex I mutants, whereas Nthy-ori 3-1 cells had wild-type mtDNA. A karyotype analysis of both HCC cell lines confirmed hyperdiploid karyotypes with additional copies of chromosomes reliably retained in HCC (chr 7, 12, 20; Supplementary Fig. S4A) consistent with the complex copy-number state. Sequencing using anchored multiplex PCR for a panel of over 100 known cancer genes found MGH-HCC1 cells to also harbor biallelic loss of *CDKN2A* and *PTEN* and NCI-HCC cells to have truncating nonsense mutations in *NF1* and *NF2*, a hot-spot *TERT* promoter variant (C228T), and partial homozygous losses of *CDKN2A* and *PTEN* (Supplementary Fig. S4B).

Having established that both HCC cell lines harbor disruptive complex I mtDNA mutations, we next characterized their bioenergetic profiles. The activity of mitochondrial complex I, but not that of complex IV, was dramatically reduced in HCC cells, whereas Nthy-ori 3-1 cells showed intact activity for both complexes (Fig. 4B). Consistent with the loss of complex I activity impairing mitochondrial NADH recycling into NAD<sup>+</sup>, the absence of pyruvate triggered a striking impairment in cell growth only in HCC cell lines (Fig. 4C; ref. 39). Because pyruvate enables cytosolic recycling of NADH into NAD<sup>+</sup>, the observed growth impairment in HCC cells can be attributed to insufficient NAD<sup>+</sup> levels. HCC cells also exhibited an extremely low baseline and uncoupled oxygen consumption rate (OCR) in comparison with Nthy-ori 3-1 and HeLa cells (Fig. 4D). This defective mitochondrial respiration was associated with very high extracellular acidification rates (ECAR), suggesting increased rates of glycolysis. We next tested if HCC cells were capable of utilizing their mitochondria to generate ATP by culturing them in glucose- or galactose-containing media, because the use of galactose as the sole sugar source forces cells to rely on OXPHOS (40). Growing the HCC cell lines in galactose confirmed their defective OXPHOS,

as this led to dramatic cell death comparable with that seen with antimycin (complex III inhibitor) treatment of Nthy-ori 3-1 cells in galactose (Fig. 4E; Supplementary Fig. S4C). Finally, NCI-HCC, but not MGH-HCC1, cells were able to form subcutaneous xenografts in NOD-SCID-IL2Rγ<sup>-/-</sup> (NSG) mice (Fig. 4F), with hematoxylin and eosin (H&E) staining and electron microscopy (EM), respectively, showing large nuclei with prominent nucleoli and abundant dysmorphic mitochondria consistent with oncocyctic pathology (Fig. 4G and H). Considering the scarcity of authentic HCC models, our HCC cell lines and the PDX model are valuable resources for the field, as they harbor the expected genetic, biochemical, and histologic features of the disease.

### CRISPR Screen Identifies Selective Essentialities in HCC

To prioritize pathways of greatest essentiality in HCC, we performed a targeted CRISPR knockout growth screen and directly compared the essentiality of key genes in NCI-HCC versus Nthy-ori 3-1 cells. We custom designed a CRISPR library to target 191 genes (Supplementary Table S5) nominated by our multidimensional profiling (75 genes), prior knowledge of mitochondrial disorders (95 genes), and experience with oncocyctic tumors (21 genes). We also targeted 50 control genes that were not differentially expressed in our HCC RNA-seq data. For positive and negative controls, we targeted 10 essential genes as well as 150 cutting and noncutting controls (Supplementary Table S5). Following infection and selection of the library in NCI-HCC and Nthy-ori 3-1 cells, serial passaging with a sampling of cells on days 5, 8, 11, 16, and 20 was performed (Fig. 5A). The single-guide RNA (sgRNA) cassette integrated into the genomic DNA was amplified from cells harvested at each time point and sequenced. The representation of each sgRNA was compared with its initial representation in cells on day 5 to derive the relative fitness of a knockout in each cell line as previously described (35). The top-scoring knockouts with reduced fitness in NCI-HCC cells [ $(Z_{\text{NCI-HCC}} - Z_{\text{Nthy-ori 3-1}})/\sqrt{2} < -2$ ] on day 11 were *GPX4*, *GAPDH*, *GABPA*, and *G6PD*, and on day 16 were *GPX4*, *GAPDH*, *HSPD1*, and *G6PD* (Fig. 5B; Supplementary Fig. S5A). Exploration of the Broad Institute’s Cancer Dependency Map showed a significant fitness reduction following *GPX4* loss in thyroid cancer cell lines, and that the thyroid lineage was the second most sensitive to *GPX4* loss of all cancer lineages tested (Fig. 5C; Supplementary Fig. S5B). This suggested that enhanced ferroptosis sensitivity was a general feature of thyroid cell lines, a finding supported by the decreased fitness of *GPX4* knockouts in Nthy-ori 3-1 cells albeit to a lesser extent than NCI-HCC cells. The striking dropout of *GPX4* knockouts in NCI-HCC cells reinforced that lipid peroxide stress is a vulnerability in HCC, which is consistent with our transcriptomic and metabolomic profiling.

The dependency on *GPX4* was noteworthy because the “Ferroptosis” gene set had one of the highest enrichment scores (Fig. 2D), and *GPX4* showed strong immunoreactivity in HCC (Fig. 2E). Closer inspection of the ferroptosis leading-edge genes revealed coordinate increases in metabolic pathways relevant to the initiation, execution, and regulation of ferroptosis (Fig. 5D; Supplementary Fig. S5C). Genes related to phospholipid (ACSLs and *LPCAT3*) and GSH (*GCLC* and *GSS*)

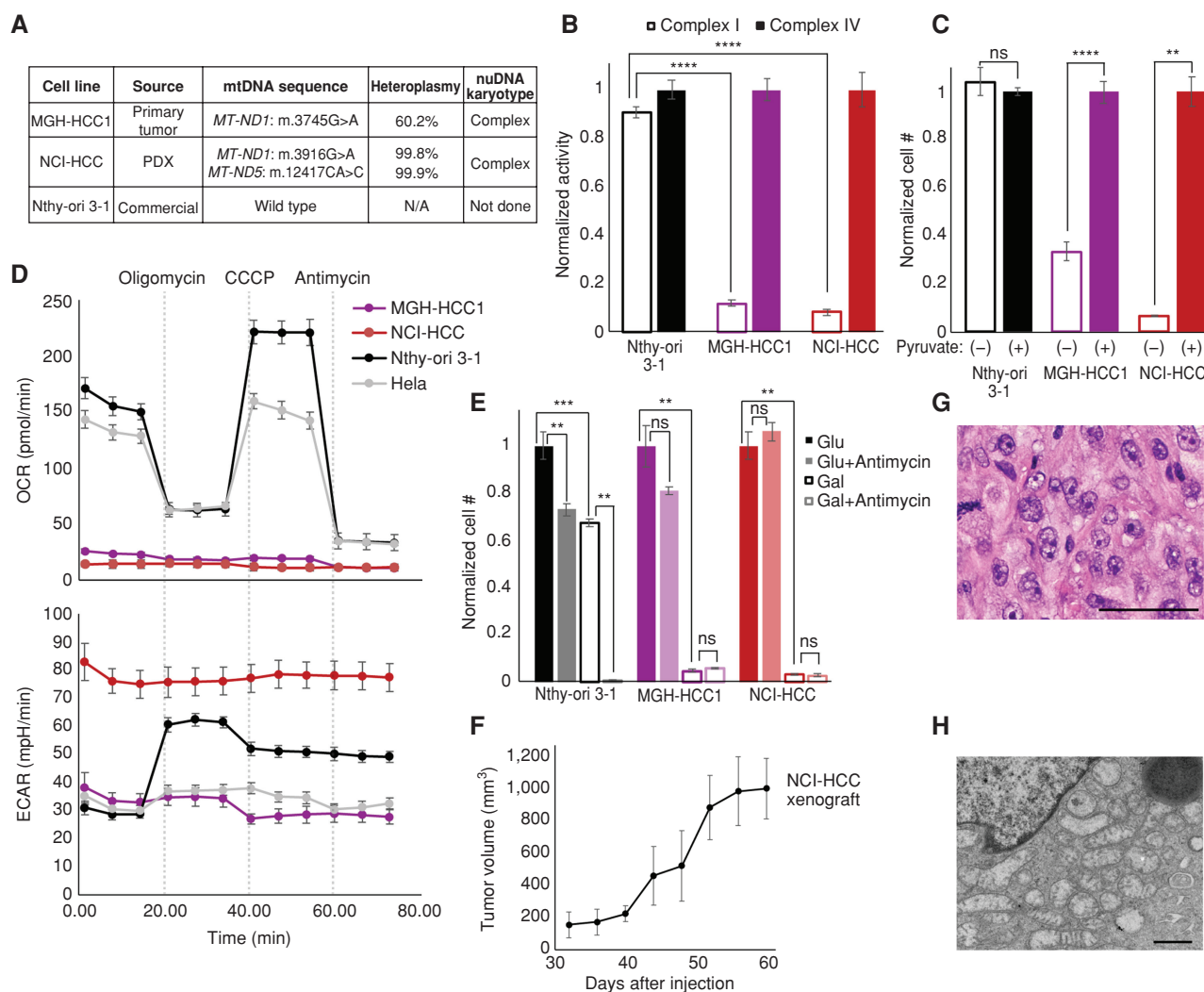


**Figure 4.** Genetics and biochemistry of authentic HCC models. **A**, Table of mtDNA mutation status and nuclear karyotype of HCC (MGH-HCC1 and NCI-HCC) and normal thyroid (Nthy-ori 3-1; immortalized via SV40 transfection) cell lines. N/A, not applicable. **B**, Normalized enzymatic activity of complex I and complex IV from cell lines. Mean  $\pm$  SD;  $n = 3$  from one experiment. **C**, Normalized cell number in media  $\pm$  pyruvate. Mean  $\pm$  SD;  $n = 2$ , representative of two experiments. **D**, OCR and extracellular acidification rate (ECAR) of cell lines from the Seahorse XFe96 Analyzer. Dotted vertical lines show drug injections. Mean  $\pm$  SD;  $n = 8-10$ , representative of 3 experiments. **E**, Normalized cell number of cell lines in glucose (Glu) or galactose (Gal)  $\pm$  antimycin. Mean  $\pm$  SD;  $n = 3$ , representative of 3 experiments. **F**, Tumor volumes ( $\text{mm}^3$ ) of NCI-HCC xenografts over time. Mean  $\pm$  SD;  $n = 3$  from 1 experiment. **G** and **H**, H&E (**G**; scale bar, 100  $\mu\text{m}$ ) and EM (**H**; scale bar, 800 nm) from NCI-HCC xenograft. For **B**, **C**, and **E**, significance tested with an unpaired t test: \*,  $P < 0.05$ ; \*\*,  $P < 0.01$ ; \*\*\*,  $P < 0.001$ ; \*\*\*\*,  $P < 0.0001$ ; ns,  $P > 0.05$ . See also Supplementary Fig. S4.

biosynthesis were increased concurrently with genes involved in free iron mobilization (*HMOX1*, *NCOA4*, *STEAP3*, *FTH1*, and *SLC40A1*) and lipid peroxide detoxification (*GPX4*; Fig. 5D). An absence of a significant change in the alternate ferroptosis suppressor *AIFM2* (also known as *FSP1*) suggests that the *GPX4* defense system may be preferentially active in HCC (Fig. 5D). The observed gene expression changes were congruent with our metabolomics showing increased biliverdin (heme metabolism) and  $\gamma$ -Glu-Cys (GSH metabolism) together with elevated PUFA-containing phospholipids (Fig. 5D). The equivalent upregulation of *ACSL4*, a gene required for ferroptosis, and *ACSL3*, a gene that protects against ferroptosis, suggests balanced incorporation of PUFAs as well as saturated and monounsaturated fatty acids (MUFA) into membrane phospholipids (Fig. 5D; refs. 41, 42). Furthermore, the significant increase in the expression of

system  $x_c^-$  members (*SLC7A11* and *SLC3A2*) underscores the importance of cystine import for GSH biosynthesis, especially because intracellular cysteine production via transsulfuration was not activated in HCC (Fig. 5D; Supplementary Fig. S3E).

### HCC Cells Are Vulnerable to *GPX4* Inhibition

We validated the sensitivity of HCC cells to *GPX4* loss using drugs that impair glutathione biosynthesis *in vivo* (sulfasalazine) or directly inhibit *GPX4 in vitro* (1S,3R-RSL 3, hereafter referred to as RSL3; Fig. 6A). Dose-response curves testing the growth impact of RSL3 in MGH-HCC1, NCI-HCC, Nthy-ori 3-1, and HeLa cells showed increased sensitivity in the three thyroid cell lines relative to HeLa cells (Fig. 6B). Moreover, MGH-HCC1 and NCI-HCC cells showed a significantly enhanced response to RSL3 compared with Nthy-ori 3-1 cells (Fig. 6B).

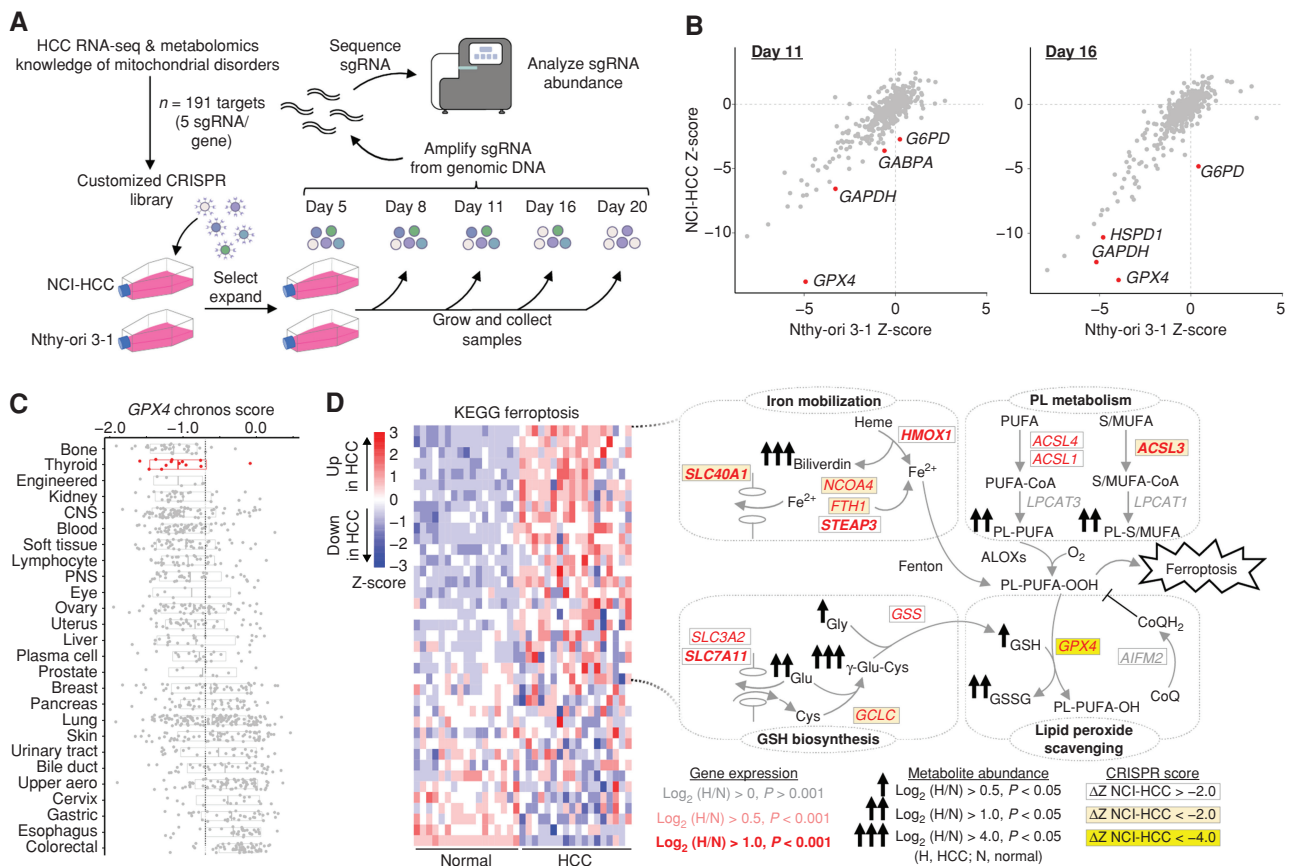


**Figure 5.** CRISPR screen identifies vulnerability to GPX4 loss in HCC. **A**, Schema for customized CRISPR screen with sampling times and DNA sequencing. **B**, Gene fitness scatter plots showing Z-scores in NCI-HCC (y-axis) vs. Nthy-ori 3-1 (x-axis) cells from day 11 and 16 time points. **C**, GPX4 chronos scores from Cancer Dependency Map for all cancer cell lines ranked by sensitivity with mean (vertical line). CNS, central nervous system; PNS, peripheral nervous system. **D**, Ferroptosis heat map with schema of metabolic pathways represented in leading-edge genes with fold changes and adjusted *P* values in genes and metabolites, as well as CRISPR fitness score annotated according to the legend. See also Supplementary Fig. S5. CoQ, coenzyme Q; CoQH<sub>2</sub>, reduced coenzyme Q; PL, phospholipid.

The toxicity induced by RSL3 could be completely rescued by the ferroptosis inhibitor ferrostatin-1, suggesting an on-target effect (Fig. 6C). In the absence of a GPX4 inhibitor with good *in vivo* bioavailability, we turned to sulfasalazine, a system  $x_c^-$  inhibitor, to establish the feasibility for targeting lipid peroxide metabolism in our NCI-HCC PDX model. NCI-HCC xenografts were treated with either vehicle or sulfasalazine (100 mg/kg) by intraperitoneal (i.p.) injection once daily after reaching ~100 mm<sup>3</sup> in size. Although the effect on tumor growth was moderate, it was notable that sulfasalazine, even as a single agent, significantly decreased the pace of tumor growth with no effect on mouse body weight (Fig. 6D; Supplementary Fig. S6A and S6B). Sulfasalazine treatment led to an increase in the levels of 4-hydroxynonenal (4-HNE), a marker of lipid peroxidation, consistent with on-target activity (Supplementary Fig. S6C). Furthermore, H&E analysis of tumors revealed that xenografts treated with sulfasalazine had increased levels of fibrosis/sclerosis, which corroborates that cysteine deprivation induced a tumor response in HCC (Fig. 6E).

### Complex I Loss Enhances Sensitivity to Ferroptosis

We next sought to determine whether it was specifically the absence of complex I activity that sensitized HCC cell lines

to GPX4 loss. Because HCC has two broad genetic defects, namely, complex I loss and widespread LOH, the vulnerability of HCC cells to GPX4 loss could in principle be mechanistically coupled to either genetic event. Prior work has suggested that electron transport chain inhibition can modulate sensitivity to GPX4 inhibition (35). We utilized genetic (NDI1) and pharmacologic (piericidin) perturbations to explore the relationship between complex I loss and ferroptosis (Fig. 7A). For our genetic approach, we stably expressed the yeast NADH dehydrogenase NDI1 (a single polypeptide) in the mitochondria of HCC and control cell lines to test if restoring the redox activity of complex I modulated the RSL3 response (43). NDI1 expression in NCI-HCC cells rescued them from pyruvate auxotrophy (Fig. 7B), illustrating that mitochondrial NAD<sup>+</sup> production was repaired, and normalized their OCR and ECAR levels, confirming that NDI1 was functioning appropriately (Fig. 7C). In terms of RSL3 sensitivity, NDI1 expression significantly right-shifted the dose response of NCI-HCC cells, suggesting that restoration of mitochondrial complex I activity augmented resistance to GPX4 inhibition (Fig. 7D). We next tested if acute inhibition of complex I activity was sufficient to confer increased sensitivity to GPX4 inhibition in a thyroid cell line with wild-type complex I. Specifically,

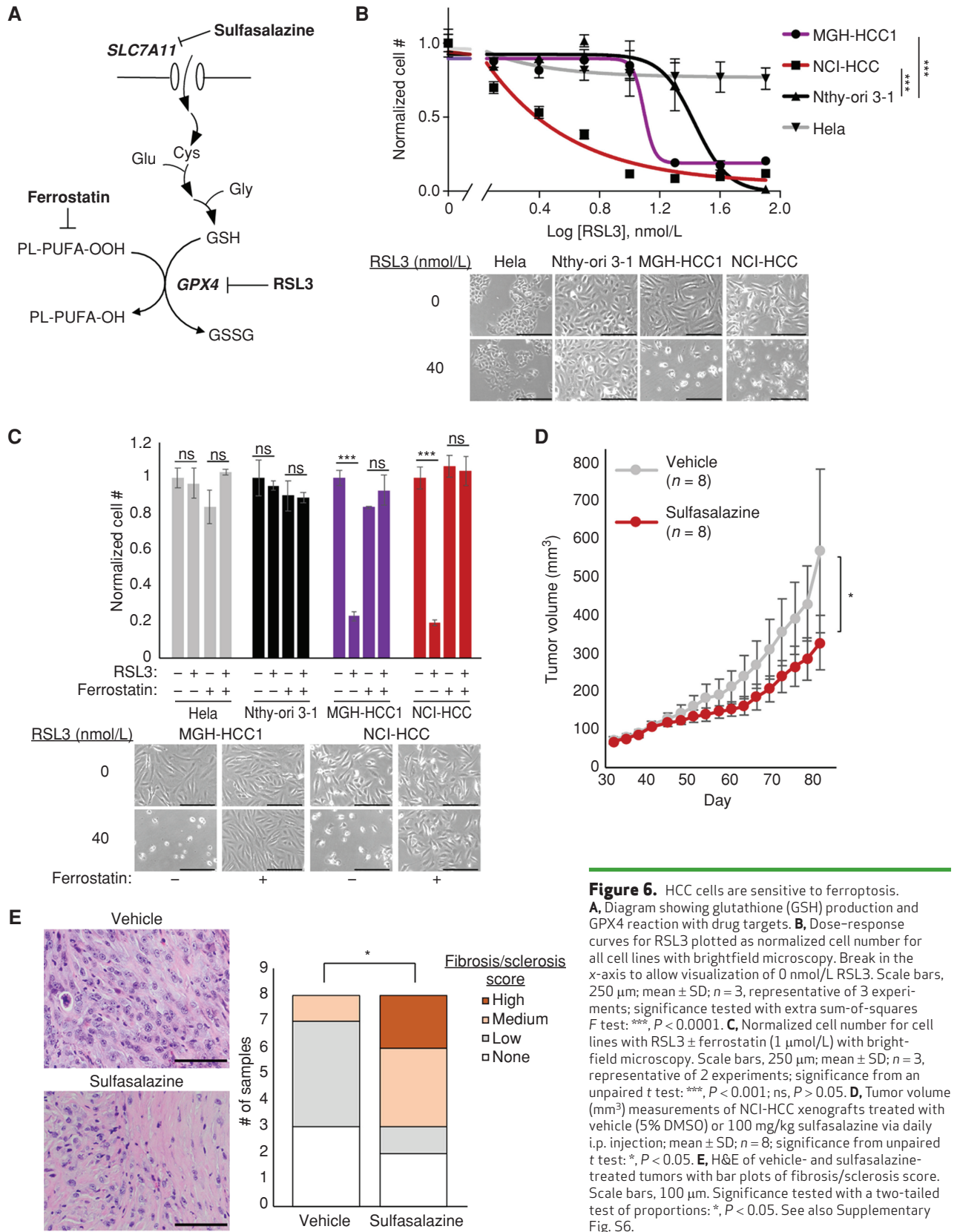
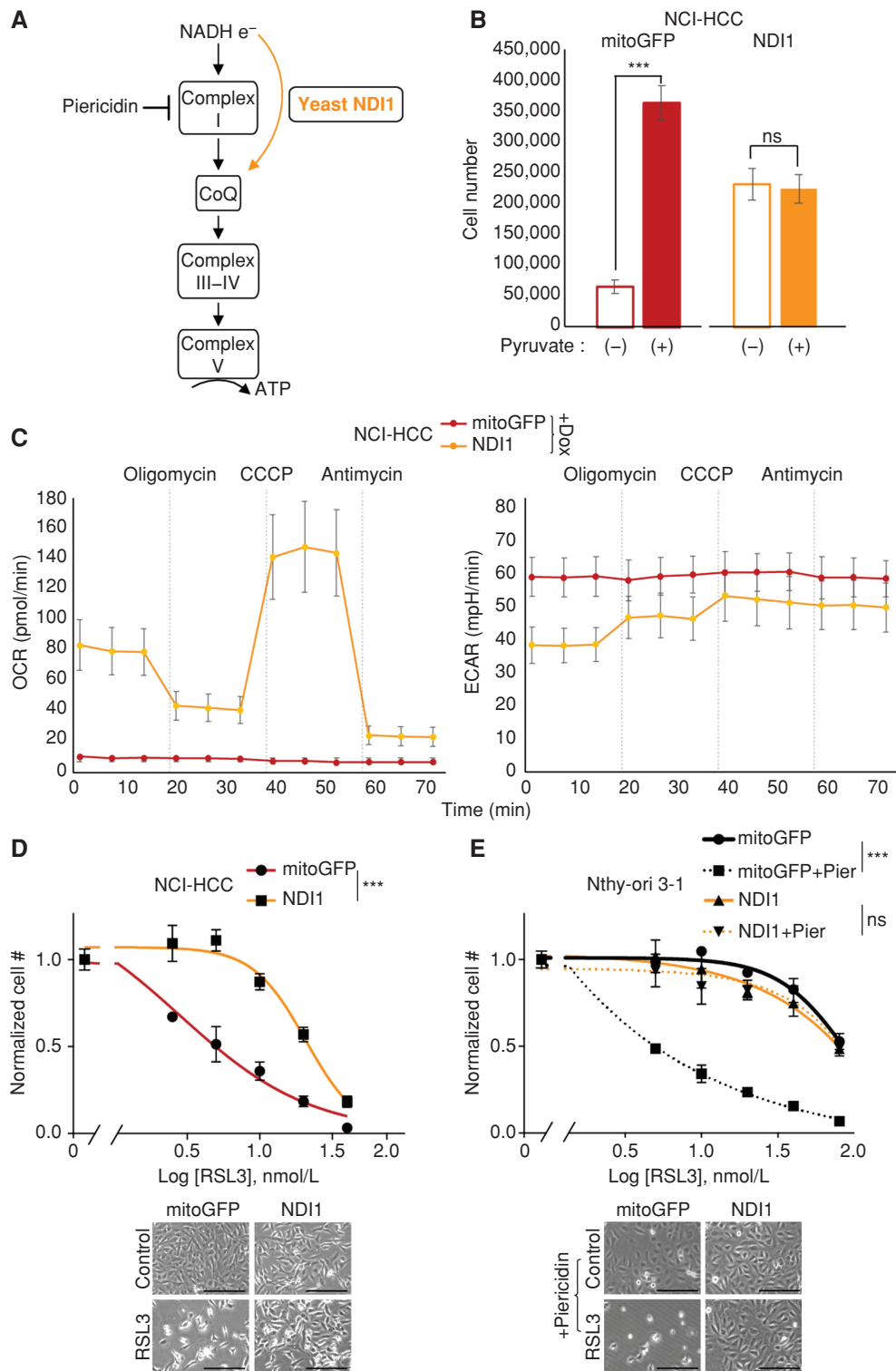


**Figure 6.** HCC cells are sensitive to ferroptosis. **A**, Diagram showing glutathione (GSH) production and GPX4 reaction with drug targets. **B**, Dose-response curves for RSL3 plotted as normalized cell number for all cell lines with brightfield microscopy. Break in the x-axis to allow visualization of 0 nmol/L RSL3. Scale bars, 250  $\mu$ m; mean  $\pm$  SD;  $n = 3$ , representative of 3 experiments; significance tested with extra sum-of-squares  $F$  test: \*\*\*,  $P < 0.0001$ . **C**, Normalized cell number for cell lines with RSL3  $\pm$  ferrostatin (1  $\mu$ mol/L) with brightfield microscopy. Scale bars, 250  $\mu$ m; mean  $\pm$  SD;  $n = 3$ , representative of 2 experiments; significance from an unpaired  $t$  test: \*\*\*,  $P < 0.001$ ; ns,  $P > 0.05$ . **D**, Tumor volume ( $\text{mm}^3$ ) measurements of NCI-HCC xenografts treated with vehicle (5% DMSO) or 100 mg/kg sulfasalazine via daily i.p. injection; mean  $\pm$  SD;  $n = 8$ ; significance from unpaired  $t$  test: \*,  $P < 0.05$ . **E**, H&E of vehicle- and sulfasalazine-treated tumors with bar plots of fibrosis/sclerosis score. Scale bars, 100  $\mu$ m. Significance tested with a two-tailed test of proportions: \*,  $P < 0.05$ . See also Supplementary Fig. S6.

Downloaded from <http://aacrjournals.org/cancerdiscovery/article-pdf/13/8/1904/3353133/1904.pdf> by guest on 15 May 2026



we treated Nthy-ori 3-1 cells with piericidin, a small-molecule inhibitor of complex I, in the context of RSL3 exposure. In line with complex I activity being mechanistically coupled to ferroptosis, acute inactivation of complex I with piericidin markedly sensitized Nthy-ori 3-1 cells to RSL3 (Fig. 7E). On the other hand, complex III inhibitors did not further sensitize Nthy-ori 3-1 cells to GPX4 inhibition (Supplementary Fig. S7A and S7B). The piericidin effect was directly due to complex I inhibition because NDI1 expression was sufficient to rescue the augmented response to RSL3. This rescue implicates mitochondrial NADH oxidation and downstream engagement of the respiratory chain in the regulation of ferroptosis (Fig. 7E). Collectively, the ability of NDI1 to decrease the sensitivity of NCI-HCC cells to GPX4 inhibition—and the ability of piericidin to sensitize Nthy-ori 3-1 cells to GPX4 inhibition—provides gain-of-function and loss-of-function evidence that causally links complex I loss to lipid peroxide sensitivity.

## DISCUSSION

Mitochondria play nuanced roles in reprogramming metabolism, a recognized hallmark of cancer (44). Comprehensive analyses of mtDNA across multiple tissue lineages suggest that damage to OXPHOS is generally selected against cancer (45, 46). Notable exceptions to this general pattern can be found in kidney, thyroid, and colon cancers, in which disruptive mtDNA mutations specifically in complex I genes accumulate at high heteroplasmy (47, 48). Oncocytic tumors, including HCC, provide unique examples of disruptive mtDNA mutations experiencing positive selection when they occur in complex I genes and suggest a need for a more balanced awareness regarding the use of complex I inhibitors in other cancers (9–11, 49). The integrated analysis presented here of the transcriptomics and metabolomics of HCC delineates the molecular consequences of complex I loss and enhances our understanding of the metabolic adaptations of these tumors. The authentic HCC cellular models described in this study validate that complex I mtDNA mutations lead to severe OXPHOS dysfunction and capture the bioenergetic profile of HCC cells. Our CRISPR–Cas9 genetic screen identifies which molecular effectors are essential in HCC and discovers a vulnerability for ferroptosis due to mitochondrial complex I loss.

The transcriptional signatures of HCC relate to well-known clinical features, including enhanced PET avidity, mitochondrial accumulation, and RAI resistance. The upregulation of genes related to glycolysis (*GAPDH*) and mitochondrial biogenesis (*ESRRA*) and the downregulation of genes involved in iodine metabolism (*SLC5A5*) provide a molecular framework for these clinical properties. The increased *GAPDH* levels are noteworthy because this glycolytic step requires  $\text{NAD}^+$ , which likely becomes limiting in the context of “reductive stress” (high  $\text{NADH}/\text{NAD}^+$  ratio) following complex I loss. The activation of mitochondrial biogenesis via increased *ESRRA* expression may work in concert with defective mitophagy stemming from complex I loss to drive the iconic display of mitochondria seen in HCC (50, 51). The enhanced mitochondrial biogenesis combined with the transcriptional features of mitochondrial dysfunction, such as increased *GDF15* and *FGF21*, heralds a mitochondrial state in HCC reminiscent of the ragged-red fiber found in mitochondrial disorders (33, 52).

The molecular alterations revealed by our study spotlight novel programs related to growth and metabolism that are enriched in HCC. The upregulation of mTOR and MYC implicates these classic oncogenic signaling paradigms as mechanisms for growth in a tumor with mtDNA mutations and chromosomal losses. The enhanced amino acid, iron, GSH, and phospholipid metabolism in HCC likely creates a metabolic mixture that further favors growth by providing biosynthetic intermediates. The activation of stress response pathways, such as the mitochondrial UPR and lipid peroxide scavenging, could act in concert with this metabolic reprogramming to protect against complex I malfunction. As complex I defects are prone to generating ROS, stimulation of GSH biosynthesis, which is what we observed in renal oncocytoma (11), may boost the ability of HCC to neutralize radical species and mitigate glutamate toxicity (53, 54).

The newly created HCC models that recapitulate defining genetic and metabolic disease features allowed us to dissect the contributions of activated molecular pathways with respect to complex I function. These models will be a valuable resource for the field moving forward, because only a single HCC cell line (XTC.UC1) with conflicting features has been reported to date (55). Our HCC cell lines display the anticipated metabolic consequences of complex I loss with their dependence on pyruvate and glucose for growth highlighting that both reductive stress and the Warburg effect are present in HCC (56, 57).

Our CRISPR–Cas9 screen allowed us to determine which molecular changes are required for cell fitness in HCC. This targeted screen revealed that *GPX4* loss is a selective vulnerability in HCC, a finding that resonates with the increased iron mobilization and PUFA phospholipids identified by our -omics profiling (58). As PUFAs preferentially undergo peroxidation, the upregulation of *GPX4* and GSH biosynthesis represents logical adaptations to detoxify these dangerous species (37). The dependence of HCC on *GPX4* is further illustrated by the marked sensitivity of our HCC cell lines to *GPX4* inhibitors. Although numerous factors, such as a high mesenchymal state, affect ferroptosis sensitivity, we discovered that a combined lineage effect together with complex I loss governs ferroptosis susceptibility in HCC (59). Cells of thyroid origin are more sensitive to *GPX4* loss than nearly all other lineages in the Cancer Dependency Map (Fig. 5C), including renal cell cancers, which have been touted for their intrinsic ferroptosis sensitivity (37). The reasons for thyroid cells preferentially relying on *GPX4* are unclear but may relate to oxidative stress due to the physiologic production of ROS during thyroid hormone production (60).

Along with the inherent lineage sensitivity, HCC displays an extreme response to *GPX4* inhibition with RSL3 due to loss of complex I redox activity (Fig. 7). The ability of mitochondria to modulate the RSL3 response is illustrated by NDI1 expression restoring the redox activity of complex I in NCI-HCC cells and rendering them more resistant to *GPX4* inhibition (Fig. 7D). Moreover, the increased sensitivity conferred by acute pharmacologic inhibition of complex I in Nthy-ori 3-1 cells further solidifies a relationship between complex I and lipid peroxidation (Fig. 7E). These experiments directly implicate mitochondrial NADH oxidation and coenzyme Q (CoQ) reduction ( $\text{CoQH}_2$ ) as proximal effectors in the regulation of ferroptosis.

The CoQ cycle serves as an additional defense system against ferroptosis that acts in parallel to GPX4. The production of CoQH<sub>2</sub> at the plasma membrane and mitochondrial inner membrane via FSP1 and DHODH, respectively, has been shown to serve as a compartment-specific radical-trapping safeguard against ferroptosis (61–63). The CoQH<sub>2</sub> system becomes the primary defense system when GPX4 is inhibited with the relative importance of the plasma membrane and mitochondrial CoQ pool depending on where lipid peroxides are formed. Our study complements the work of Mao and colleagues in establishing a role for enzymes capable of donating electrons to CoQ (DHODH and complex I) in modulating ferroptosis sensitivity (63). As the major flow of electrons into the mitochondrial CoQ pool is typically driven by complex I (64), it is important to consider this first step in mitochondrial respiration as a mechanism for fine-tuning the response to lipid peroxides. The exquisite sensitivity of HCC to GPX4 inhibition may result from complex I loss decreasing CoQH<sub>2</sub> levels and thereby increasing the reliance on the mitochondrial GPX4 isoform to cope with the mitochondrial membrane stress associated with HCC.

Emerging data establish a clear role for GPX4 in mitochondria (35, 65) despite ferroptosis being considered a distinct form of cell death independent of the mitochondrial respiratory chain (66). In addition to the long isoform of GPX4 localizing to the mitochondrial inner membrane, GPX4 has been reliably found in the mitochondria of all 14 mouse tissues as reported in MitoCarta3.0 (23, 35, 67). Although earlier studies suggested that mitochondria are not required for ferroptosis, this notion was based on observations from cells with depleted mtDNA or activated mitophagy (66, 68). Subsequent data have shown that electron transport chain activity promotes ferroptosis during cysteine depletion (69), and work from our lab illustrates that electron transport chain inhibition creates a strong dependence on GPX4 (35). This interaction of the respiratory chain and GPX4 along with the findings of these studies implicates mitochondria in ferroptosis regulation, with the extent of this contribution deriving from an interplay of genetics, lineage, and compartmental source of membrane peroxidation (63).

Our work highlights the selective importance of GPX4 for maintaining cell fitness in HCC. We directly connect the essentiality of GPX4 to the loss of mitochondrial complex I and show how modulation of the redox activity of complex I is sufficient to regulate ferroptosis sensitivity. At present, highly potent and specific GPX4 inhibitors with favorable *in vivo* pharmacokinetics/pharmacodynamics are lacking. Once developed, they could potentially be used in HCC based on our results. We also envision future studies leveraging the lineage and complex I effects that we have described in rational ways to broadly treat other types of cancers. Ferroptosis-inducing agents may also be an attractive strategy for other aggressive thyroid cancers, capitalizing on the profound lineage effect that we observed. Because patients with metastatic thyroid cancer will have had all normal thyroid cells ablated, either surgically or with RAI, the lineage effect of GPX4 inhibition can be leveraged strategically without concern for toxicity to the normal thyroid gland. Finally, because complex I mtDNA mutations have been described in other cancers, genotyping the mtDNA could be an effective precision medicine strategy to nominate the use of a ferroptosis inducer in a patient-specific manner (11, 47).

## METHODS

### Human Tissue Studies

HCC samples were collected and stored with approval of the Mass General Brigham Institutional Review Board (protocol number 2008P001466). Studies were conducted in accordance with recognized ethical guidelines after obtaining written informed consent from patients. Frozen tissue was accessed to create the cohort used in this study, and clinical annotations are included in Supplementary Table S1. Frozen samples were processed for RNA-seq and metabolomics at the Broad Institute.

### Mouse Studies

Female NSG (The Jackson Laboratory; RRID: IMSR\_JAX:005557) mice of 4 to 6 weeks of age were purchased and housed at the animal care facility at Massachusetts General Hospital (MGH). All procedures were approved by the MGH Institutional Animal Care and Use Committee and conformed to NIH guidelines. Cohorts of xenografts were created to account for a 10% attrition rate, and experimental groups were randomly assigned after tumors were established. Tumor size was tracked with digital calipers, and mouse weights were recorded using a digital scale throughout the experiment.

### Cell Culture Studies

The MGH-HCC1 cell line (source: male) was derived from a resected metastasis from a patient in this cohort. The NCI-HCC cell line (source: male) was derived from a tumor grown from PDX material obtained from the NCI Patient-Derived Models Repository (model 248138-237-R). The Nthy-ori 3-1 cell line (source: female) was purchased (Sigma; cat. #90011609) and was part of the European Collection of Authenticated Cell Cultures. All cell lines were grown in humidity-controlled incubators at 21% O<sub>2</sub>, 5% CO<sub>2</sub>, and 37°C and routinely tested for *Mycoplasma* (Lonza; cat. #LT07-218; last tested February 16, 2023). Cell lines were authenticated using the ATCC short tandem repeat authentication method (ATCC; cat. #135-XV), and early passage freezer stocks were used for all experiments. MGH-HCC1 and NCI-HCC cells were routinely passaged in DMEM-11995 (Thermo Fisher; cat. #11995073) media with 10% fetal bovine serum (FBS) and 50 µg/mL uridine. Nthy-ori 3-1 and Hela cells (source: female; ATCC; cat. #CCL2) were routinely passed in RPMI 1640 media (Sigma; cat. #R8758) with 10% FBS. All experiments were conducted in DMEM-11995 media with 10% FBS and 50 µg/mL uridine unless otherwise specified.

### mtDNA Sequencing

Genomic DNA (100 ng) from HCC samples and cell lines was amplified with a two-amplicon long-range PCR method (70, 71). A TaKaRa LA Hot-Start Taq DNA polymerase (TaKaRa Clontech; cat. #RR042A) was used with the following cycling parameters: 95°C for 2 minutes, followed by 28 cycles of 95°C for 20 minutes, 68°C for 10 minutes, and concluding with 10 minutes at 72°C. PCR products were purified using AMPure XP beads (Beckman Coulter; cat. #A63880), sheared into 200 bp fragments with a COVARIS sonicator, and sequenced using an MiSeq reagent kit v3 (150 cycles; Illumina; cat. #MS-102-3001) with 75 bp paired-end reads. All reads mapping to GRCh37 chromosome MT were aligned to the revised Cambridge Reference Sequence (NC\_012920) using GATK version 3.3 (RRID:SCR\_001876), BWA version 0.7.12 (RRID:SCR\_010910), and Picard Tools version 1.100. Somatic mtDNA variants were detected using the GATK HaplotypeCaller assuming a 20-chromosome mixture. Nonsynonymous somatic variants of potential pathologic significance were identified using the following filters: (i) depth in tumor and matched normal (when available)  $\geq 15\times$ ; (ii) variant allelic fraction (VAF)  $>0.3$  in tumor and  $<0.05$  in matched normal; and (iii) tumor VAF - normal VAF  $>0.4$ . For tumors without matched normal tissue, we reported loss-of-function variants, the MT-TL

3244G>A variant associated with MELAS, and a missense variant in HC024 that was also reported in our whole-exome cohort as pathogenic (9). Variants deemed to be pathogenic were validated by RNA-seq reads for the corresponding mtRNA species using samtools (RRID:SCR\_002105) mpileup and a custom R script to determine the proportions of reference and alternate alleles. A mutation was considered validated if the RNA-seq heteroplasmy was >10%. Large mtDNA deletions were identified by analyzing the uniformity of coverage for all tumor samples. For cell line mtDNA analysis, variants were considered pathogenic if they resulted in nonsynonymous changes, had a VAF >0.1, and were not associated with an mtDNA haplogroup.

### aCGH Analysis

Genome-wide copy-number variations were assessed using the SurePrint G3 Human aCGH 4 × 180K Microarray (Agilent Technologies; cat. #G4890A; RRID:SCR\_013575) according to the manufacturer's recommendations. Briefly, 1 µg of tumor DNA extracted from fresh-frozen tissue and 1 µg of male human reference DNA control were digested with *AluI* and *RsaI*. After restriction digestion, the sample DNA and the control DNA were individually labeled by random priming with CY5-dUTP and CY3-dUTP, respectively, using the SureTag DNA labeling kit (Agilent Technologies). The labeled DNAs from tumors and controls were purified, mixed in equal amounts, and hybridized to the microarray for 35 to 40 hours at 65°C using the Oligo aCGH Hybridization Kit (Agilent Technologies). Following hybridization, the slides were washed and scanned using the G2565A Microarray Scanner (Agilent Technologies). Microarray TIFF (.tif) images were processed with Agilent Feature Extraction Software v12.0. Array data were analyzed using the Agilent CytoGenomics 2.7 software (RRID:SCR\_010917). Of note, the CytoGenomics software assumes the majority of chromosomal material in a mosaic sample is diploid. As a result, for tumor samples with a higher proportion of chromosomal haploidy than diploidy, the automatic analysis did not pass quality control (QC) and yielded unusual SNP probe distributions. For these samples, we used manual reassignment of copy-number values for the different aCGH log ratio populations and reanalyzed the data. For tumor samples with a larger proportion of haploid material, this manual approach followed by the CytoGenomics software analysis yielded the expected SNP profiles and QC metrics that fell within the preferred range.

### RNA-seq and Data Analysis

RNA samples were prepared and sequenced at the Broad Institute using a standard large insert strand-specific mRNA sample preparation kit (TruSeq stranded mRNA) with poly(A) selection. Total RNA was quantified using the Quant-iT RiboGreen RNA Assay Kit and normalized to 5 ng/µL. Following plating, 2 µL of ERCC controls (1:1,000 dilution) were spiked into each sample. A 200-ng aliquot of each sample was transferred into library preparation using an automated variant of the Illumina TruSeq Stranded mRNA Sample Preparation Kit. Following heat fragmentation and cDNA synthesis, the resultant 400 bp cDNA was then used for dual-indexed library preparation, which included "A" base addition, adapter ligation using P7 adapters, and PCR enrichment using P5 adapters. After enrichment, the libraries were quantified using Quant-iT PicoGreen (1:200 dilution). After normalizing samples to 5 ng/µL, the set was pooled and quantified using the KAPA Library Quantification Kit for Illumina Sequencing Platforms. Pooled libraries were normalized to 2 nmol/L and denatured using 0.1 N NaOH prior to sequencing. Flow cell cluster amplification and sequencing were performed according to the manufacturer's protocols using either the HiSeq 2000 or HiSeq 2500. Each run was a 101 bp paired-end with an eight-base index barcode read. RNA reads were aligned to the reference genome (hg19) using a STAR aligner and demultiplexed and aggregated into a Picard BAM file.

After alignment, RSeQC and PicardTools BamIndexStats were run on the BAM files to assess the quality of the samples. Several samples were

excluded from RNA-seq analyses based on the QC metrics. HC004\_N (N, normal) had high PCR duplicates, and 5% contamination was detected. Several tumor samples were excluded due to low and uneven coverage: HC001\_T (T, tumor), HC005\_T, HC007\_T, HC010\_T, and HC019\_T. Additionally, for transcriptomic analyses, HC012\_T was excluded because of the large 3.7 kb deletion in the mtDNA. Raw counts were estimated from alignment files using featureCounts from the Subread package (RRID:SCR\_016945). Counts were normalized using the R package qsmooth, which normalizes assuming both global variation in samples and variation within conditions (72). Linear regression was performed on these normalized counts after transforming with voom using the R package limma. The matrix of normalized counts was the outcome variable for the regression, and tumor/normal status was the predictor. Age, sex, and body mass index (BMI) were not used as covariates, as qsmooth was used to quantile normalize counts and account for these differences in groups. Because all experiments were performed in a single batch, we did not correct for batch. However, we did account for intersample correlation introduced by the paired nature of the samples by using the individual as a blocking factor.

### GSEA

Because GSEA (RRID:SCR\_005724) requires that features be comparable both within and between samples, fragments per kilobase of exon per million mapped fragments (FPKM; as calculated from raw counts) was used as input for GSEA. DESeq2 (RRID:SCR\_015687) was used to transform raw counts to FPKM (73). GSEA was performed for eight databases of gene sets: h.all.v7.1.symbols.gmt (HALLMARK), c1.all.v7.1.symbols.gmt (Positional), c2.all.v7.1.symbols.gmt (Curated), c2.cp.kegg.v7.1.symbols.gmt (Curated), c3.all.v7.1.symbols.gmt (Motif), c5.all.v7.1.symbols.gmt (Gene Ontology), c6.all.v7.1.symbols.gmt (Oncogenic signatures), and c7.all.v7.1.symbols.gmt (Immunologic signatures). GSEA was also performed on a curated version of the KEGG gene set that focused on metabolic pathways: c2.cp.kegg.v7.1.symbols.gmt. Each analysis was done in the desktop version of GSEA 4.0, with 1,000 permutations of phenotype labels. All other settings were as per GSEA defaults.

### Metabolomics

Fresh-frozen normal thyroid and HCC samples were submitted for processing and mass spectrometry at the Broad Metabolomics platform. Tissues were weighed and homogenized in 4 volumes of water (4 µL of water/mg tissue, 4°C) using a bead beater (TissueLyser II, Qiagen). Aqueous homogenates were profiled using four complementary LC-MS methods. Hydrophilic interaction liquid chromatography analyses of water-soluble metabolites in positive and negative ionization mode were conducted using an LC-MS system comprised of a Shimadzu Nexera X2 U-HPLC (Shimadzu Corp.) coupled to a Q Exactive and Q Exactive Plus mass spectrometer, respectively (Thermo Fisher Scientific). Metabolites were extracted and injected as previously described (74). In the negative ion mode, MS analyses were carried out using electrospray ionization using full scan analysis over *m/z* 70 to 750 at 70,000 resolution and 3 Hz data acquisition rate. Additional MS settings were as follows: ion spray voltage, -3.0 kV; capillary temperature, 350°C; probe heater temperature, 325°C; sheath gas, 55; auxiliary gas, 10; and S-lens RF level 50. Lipids were profiled using a Shimadzu Nexera X2 U-HPLC (Shimadzu Corp.) as previously described (74). Lipid identities were denoted by the total acyl carbon number and the total number of double bond numbers. Metabolites of intermediate polarity, including free fatty acids and bile acids, were profiled using a Shimadzu Nexera X2 U-HPLC (Shimadzu Corp.) coupled to a Q Exactive (Thermo Fisher Scientific). Homogenates (30 µL) were extracted and injected as previously described (74).

Raw data were processed using TraceFinder 3.3 software (Thermo Fisher Scientific) and Progenesis QI (Nonlinear Dynamics). For each method, metabolite identities were confirmed using authentic reference standards or reference samples.

We excluded samples from analysis for low tissue yield, or if they had poor mtDNA sequencing results (indicating general poor sample quality). Metabolites were filtered if they had less than 1,000 IU average intensity across both tumors and normal samples, indicating a potentially unreliable signal. Metabolites were also filtered if they were not consistently detected in the pooled QC samples, indicating a potentially unreliable signal. Data were then  $\log_{10}$  transformed after the addition of a very small value to avoid taking the log of 0.

The log-transformed metabolite levels were used as the outcome in a multiple multivariate regression with the R package *limma* (RRID:SCR\_010943), using status as a predictor and age, sex, and BMI as covariates (75). The intercorrelation within an individual was accounted for using blocking.

### PDX and Cell Line

The MGH-HCC1 cell line was derived from a resected metastasis (HC024) and cultured in DMEM-11995 media with 10% FBS and 50 mg/mL uridine. The tumor sample was cut into small pieces and trypsinized with pipetting to break up tissue chunks then spun at 1,200 rpm for 5 minutes in a Beckman Coulter Allegra X-12/R centrifuge. The pellet was resuspended and then passed through a cell strainer and plated into 6-well plates at 21% O<sub>2</sub>, 5% CO<sub>2</sub>, and 37°C. Cells were then monitored with microscopy to track morphology and serially passaged with differential trypsinization until an immortalized cell line with epithelial morphology resulted.

The NCI-HCC cell line derived from a PDX model developed by the NCI Patient-Derived Models Repository (model 248138-237-R). A tumor grown from transplanted xenograft tissue from the NCI PDMR was harvested, cut into small pieces, and digested with collagenase. Digested material was then passed through a cell strainer and grown in DMEM-11995 media with 10% FBS in incubators kept at 21% O<sub>2</sub>, 5% CO<sub>2</sub>, and 37°C. Cells were serially passaged until an immortalized cell line was established that retained the ability to form xenografts in NSG mice.

Karyotyping of the MGH-HCC1 and NCI-HCC cell lines was performed at the Brigham and Women's Hospital CytoGenomics Core Laboratory. The karyotype was analyzed using the GTG banding pattern and counting 20 metaphase spreads with further analysis of five karyotypes with marker chromosome evaluation. Targeted next-generation sequencing using a customized version of the VariantPlex Solid Tumor Kit (ArcherDX Inc.) was performed to look for variants in 104 known cancer genes in MGH-HCC1 and NCI-HCC cells as previously described (76). Briefly, enzymatically sheared double-stranded genomic DNA was end-repaired, adenylated, and ligated with a half-functional adapter. Next-generation sequencing using Illumina NextSeq 2 × 150 was performed on a sequencing library made from two hemi-nested PCR reactions.

### OXPPOS Activity and OCR Assays

Complex I (Abcam; cat. #ab109721) and complex IV (Abcam; cat. #ab109909) enzyme activity assays were performed on lysates from MGH-HCC1, NCI-HCC, and Nthy-ori 3-1 cells. For each assay, 1 × 10<sup>7</sup> cells were harvested, washed, and resuspended according to the manufacturer's protocol and the protein concentration was determined using BCA. Microplates were loaded with samples and incubated for 3 hours at room temperature for each assay. After washing and adding the respective assay solutions, the plates were placed in an Envision microplate reader, and the enzyme activity was measured at 450 nm (complex I) and 550 nm (complex IV). OCR and ECAR were measured in cell lines using a Seahorse XFe96 Analyzer (Agilent). Cell lines were seeded at 30,000 cells/well in standard culture media. The next day, the media were changed to media of the same formulation (25 mmol/L glucose, 4 mmol/L glutamine, and 1 mmol/L pyruvate) except with HEPES-KOH substituted for sodium bicarbonate and with no phenol red present. Cells were placed for 1 hour into

a non-CO<sub>2</sub> controlled incubator at 37°C and then transferred to the Seahorse XFe96 Analyzer for OCR and ECAR measurements. Inhibitors were added from ports to achieve the following concentrations: oligomycin (Sigma; cat. #75351) 1.5 μmol/L, CCCP (Sigma; cat. #C2759) 2 μmol/L, and antimycin (Sigma, cat. #A8674) 0.5 μmol/L. The same Seahorse protocol was used for NCI-HCC cells expressing mitochondrial-localized GFP (mitoGFP) or NDI1, except doxycycline (Alfa Aesar; cat. #J60579) 1 μg/mL was added to the media.

### Cell Growth and Drug Testing

For growth assays testing the effect of pyruvate, MGH-HCC1, NCI-HCC, and Nthy-ori 3-1 cells were cultured in DMEM 11965 media with 10% dialyzed FBS (Thermo Fisher; cat. #26400044) and 1 mmol/L sodium pyruvate. Cells were then seeded in triplicate at 30,000 cells/well into 6-well plates with DMEM 11965 media with 10% dialyzed FBS ± 1 mmol/L sodium pyruvate. Cells were then harvested after 4 days and counted. The same protocol was followed with NCI-HCC cells expressing either mitoGFP or NDI1, except cells were seeded in triplicate at 100,000 cells/well in doxycycline (0.5 μg/mL) with uridine 50 μg/mL ± 1 mmol/L sodium pyruvate and harvested 3 days later. All cell counts were done using a Z2 Coulter Particle Count and Size Analyzer (Beckman Coulter) and plotted as either normalized to the average cell number with pyruvate present for each cell line or as the total cell number.

For growth assays testing the effect of glucose versus galactose, MGH-HCC1, NCI-HCC, and Nthy-ori 3-1 cells were seeded in triplicate at 100,000 cells/well in 6-well plates in standard passaging media. The next day, cells were washed twice with PBS and then grown in DMEM 11966-025 media with either 10 mmol/L glucose or 10 mmol/L galactose, 10% dialyzed FBS, 1 mmol/L sodium pyruvate, and 50 μg/mL uridine ± 1 μmol/L antimycin. Cells were harvested after 3 days and counted using a Z2 Coulter Particle Count and Size Analyzer (Beckman Coulter).

For growth assays testing the effect of RSL3 (Sigma; cat. #SML2234), MGH-HCC1, NCI-HCC, Nthy-ori 3-1, and Hela cells were seeded in triplicate at 15,000 cells/well in 24-well plates in DMEM-11995 media with 10% FBS and 50 μg/mL uridine. The next day, cells were exposed to serial dilutions of RSL3 or DMSO. After 3 days of drug exposure, cells were harvested and counted using a Z2 Coulter Particle Count and Size Analyzer (Beckman Coulter). For ferrostatin rescue experiments, cells were plated as above and then pretreated with ferrostatin (1 μmol/L; Sigma; cat. #SML0583) for ~1.5 hours before exposing to RSL3 (40 nmol/L). Cells were exposed to RSL3 ± ferrostatin for 3 days prior to harvesting and counting. For all growth assays, brightfield microscopy images were taken using a Qimaging QICAM FAST 1394 digital camera at 4× magnification.

### CRISPR Screen

A customized CRISPR library targeting 191 genes of interest, 50 control genes, and 10 essential genes with five sgRNAs per gene as well as 75 noncutting and 75 cutting controls was generated at the Broad Institute. The library was cloned into an "all-in-one" (pXPR\_023) vector expressing the sgRNAs and SpyoCas9. Spin infections of NCI-HCC and Nthy-ori 3-1 cells were performed in 12-well plates with 500,000 cells/well to achieve a multiplicity of infection (MOI) of 0.3 to 0.5. Optimal conditions for infection were empirically determined by infecting cells with different volumes of virus (0, 60, 80, 100, 120, and 160 μL) with polybrene (0.8 μg/mL; Sigma; cat. #H9268) in each cell line. Cells were centrifuged for 1 hour at 931 × g at 30°C. Approximately 24 hours later, cells were harvested and transferred to 6-well plates and exposed to either vehicle or puromycin (Thermo Fisher, cat. #A1113803). Cells were then counted 48 hours later to determine the virus volume that yielded an MOI of 0.3 to 0.5.

A screening-scale infection was then performed in NCI-HCC and Nthy-ori 3-1 cells with the empirically determined optimal virus amount in 12-well plates (500,000 cells/well). Infections were

performed to reach a library representation of ~1,000 cells/guide following puromycin selection. The day after infection, all wells from each cell line were pooled and exposed to puromycin (2.0 µg/mL) for 48 hours. After selection was complete, cells were passaged in 175 cm<sup>2</sup> T flasks and genomic DNA was isolated on days 5, 8, 11, 16, and 20 after infection using a NucleoSpin kit (Takara; cat. #740951.5). PCR was performed as previously described and samples were sequenced on a MiSeq sequencer (Illumina; refs. 35, 77). Raw sgRNA counts were normalized and transformed according to the formula:  $\text{Log}_2(\text{reads from an individual sgRNA}/\text{total reads in the sample} \times 10^6 + 1)$ . The relative fitness of a knockout was determined according to the formula  $(\Delta Z_{\text{day}\#} = Z_{\text{NCI-HCC day}\#} - Z_{\text{Nthy-ori 3-1 day}\#})/\sqrt{2}$ , where the Z-score is based on the log<sub>2</sub> fold change of normalized sgRNA count for a given day # relative to day 5. Top-scoring knockouts were identified by comparing the relative fitness in NCI-HCC and Nthy-ori 3-1 cells and defined as  $\Delta Z_{\text{day}\#} < -2$ .

### Xenograft Assays

For tumor growth assays,  $2 \times 10^6$  cells were injected subcutaneously in Matrigel (Corning; cat. #356231) into the flank of NSG mice. Mouse weights were tracked with digital scales, and tumor size was measured using digital calipers every 3 to 4 days, with volumes calculated from the formula  $\text{volume} = \frac{1}{2}(\text{length} \times \text{width}^2)$ . Once tumors reached a target volume of 100 mm<sup>3</sup>, a cohort of 16 mice was randomized in equal numbers to vehicle or sulfasalazine (Sigma; cat. #S0883) to have 80% power to detect a 2-fold difference in growth with 25% standard deviation of tumor volumes and a 5% two-sided significance level (two-sample *t* test). Vehicle (5% DMSO in saline) and sulfasalazine (100 mg/kg in 5% DMSO in saline) were injected i.p. daily. Sulfasalazine was dissolved in DMSO and diluted in saline prior to injection. 4-HNE levels were assessed using a Western blot with a primary antibody (Sigma; cat. #393206) and quantified using the Fiji image processing package, with Coomassie staining used as a loading control.

### IHC and EM

Formalin-fixed, paraffin-embedded human normal thyroid and HCC samples as well as tumor xenografts were processed for IHC at the MGH Histopathology Core as previously described (11). The following primary antibodies were used: GRP75 (Cell Signaling Technology; cat. #3593, RRID:AB\_2120328, 1:50); S6 (Cell Signaling Technology; cat. #2217, RRID:AB\_331355, 1:150); phospho-S6 ser 235/236 (Cell Signaling Technology; cat. #2211S, 1:400); GPX4 (Abcam; cat. #ab125066, RRID:AB\_10973901, 1:100); and 4-HNE (Abcam; cat. #ab46545, RRID:AB\_722490, 1:100). All stained slides were evaluated and scored by an expert pathologist in a blinded fashion.

EM of xenograft tissue was performed at the MGH Program in Membrane Biology microscopy core facility. Xenograft tissue pieces were fixed overnight in 2% paraformaldehyde/2.5% glutaraldehyde in 0.1 M sodium cacodylate buffer (pH 7.4), washed, infiltrated 1 hour in 1% osmium tetroxide, washed, and then dehydrated into 100% propylene oxide. Samples were incubated in a mix of propylene oxide:Eponate resin (Ted Pella), placed into a 2:1 mix of Eponate:propylene oxide ( $\geq 2$  hours), transferred into fresh 100% Eponate, and polymerized in flat molds in a 60°C oven (24–48 hours). Ultrathin (70 nm) sections were cut using a Leica EM UC7 ultramicrotome, collected onto formvar-coated grids, stained with 2% uranyl acetate and Reynold's lead citrate, and examined in a JEOL JEM 1011 transmission electron microscope at 80 kV. Images were collected using an AMT digital imaging system with proprietary image capture software (Advanced Microscopy Techniques).

### NDI1 Expression

A Tet-On 3G inducible expression system for mitoGFP and NDI1 was established in NCI-HCC and Nthy-ori 3-1 cells. The NDI1 protein contained an N-terminal FLAG tag after the mitochondrial targeting

sequence (39). Both cell lines were initially infected with the pLVX-Tet3G (Clontech; cat. #631193) regulator vector and then underwent selection with Geneticin (1 mg/mL). Surviving cells were then infected with lentivirus for either mitoGFP or NDI1 expressed in the pLVX-TRE3G (Clontech; cat. #631359) response vector and selected with puromycin (2 µg/mL).

### Statistical Analysis

For all analyses, significance was determined at  $P < 0.05$ . \*, \*\*, and \*\*\* represent varying degrees of significance between groups as defined in the figure legends. To study the differences between the two groups, a Student *t* test was utilized to look for significance. For dose–response curves, significant differences in the LogIC<sub>50</sub> value were assessed using an extra sum-of-squares *F* test after performing a least squares regression curve fit of the data. Randomization of mouse xenografts prior to starting drug treatments was done using a randomization function in Microsoft Excel (RRID:SCR\_016137). Figure legends define *n*, the number of times an experiment was performed, and what center and dispersion values are shown. For *in vivo* studies, *n* defines the number of biological replicates, and for *in vitro* studies, *n* defines the number of replicate wells. All analyses were performed in Microsoft Excel (Version 16.54), GraphPad Prism (Version 9.3.1; RRID:SCR\_002798) or using R code. The line and box for genes and metabolites represent the mean and standard deviations.

### Data Availability

Further information and requests for resources and reagents should be directed to and will be fulfilled by the lead contact, V.K. Mootha (vamsi\_mootha@hms.harvard.edu). Cancer cell lines generated in this study are available upon request. Bulk RNA-seq and metabolomics data have been deposited at the Gene Expression Omnibus (accession #GSE228870) and the National Metabolomics Data Repository (accession #PR001632), and are publicly available as of the date of publication.

### Authors' Disclosures

B. Reimer reports other support from Novartis Institutes of BioMedical Research outside the submitted work. P.M. Sadow reports grants from the NIH/NCI during the conduct of the study. L.J. Wirth reports personal fees from Bayer HealthCare, Coherus, Curie Therapeutics, Eli Lilly, Eisai, Exelixis, Genentech, Merck, Morphic Therapeutics, and Tome Biosciences outside the submitted work. S. Parangi reports grants from the Bertarelli Foundation and the Ruane Foundation during the conduct of the study. V.K. Mootha reports other support from the Ruane Foundation and Howard Hughes Medical Institute, and grants from the Bertarelli Rare Cancers Fund during the conduct of the study, as well as personal fees and other support from 5am Ventures and personal fees from Janssen Pharmaceuticals outside the submitted work. No disclosures were reported by the other authors.

### Authors' Contributions

**R.K. Gopal:** Conceptualization, resources, data curation, formal analysis, investigation, methodology, writing—original draft, writing—review and editing. **V.R. Vantaku:** Investigation. **A. Panda:** Formal analysis. **B. Reimer:** Formal analysis. **S. Rath:** Methodology. **T.-L. To:** Methodology. **A.S. Fisch:** Investigation. **M. Cetinbas:** Formal analysis. **M. Livneh:** Methodology. **M.J. Calcaterra:** Project administration. **B.J. Gigliotti:** Data curation. **K.A. Pierce:** Investigation. **C.B. Clish:** Investigation. **D. Dias-Santagata:** Investigation. **P.M. Sadow:** Investigation. **L.J. Wirth:** Supervision. **G.H. Daniels:** Supervision. **R.I. Sadreyev:** Supervision. **S.E. Calvo:** Formal analysis, supervision. **S. Parangi:** Conceptualization, resources, supervision, administration. **V.K. Mootha:** Conceptualization, resources, supervision, project administration, writing—review and editing.

## Acknowledgments

We thank the Brigham and Women's Hospital (BWH) CytoGenomics Core Laboratory, BWH Department of Pathology. The CRISPR-Cas9 library was designed and produced by Adam Brown, Amy Goodale, and David Root at the Genetic Perturbation Platform at the Broad Institute. Electron microscopy was performed in the Microscopy Core of the Center for Systems Biology/Program in Membrane Biology, which is partially supported by an Inflammatory Bowel Disease Grant (DK043351) and a Boston Area Diabetes and Endocrinology Research Center Award (DK057521). We thank Ivy Rosales, Andrea Rios, and Christina Laguerre from the Mass General Histopathology Research Core Laboratory, as well as Yoshiko Iwamoto from the Mass General Center for Systems Biology. This work was supported by the Bertarelli Rare Cancers Fund and a generous gift from the Elizabeth and Michael Ruane family. B.J. Gigliotti was supported by 2T32DK007028-46. S. Rath was supported by NIH K00CA212468. R.K. Gopal was supported by NIH K12CA087723. V.K. Mootha is an investigator at the Howard Hughes Medical Institute.

The publication costs of this article were defrayed in part by the payment of publication fees. Therefore, and solely to indicate this fact, this article is hereby marked "advertisement" in accordance with 18 USC section 1734.

## Note

Supplementary data for this article are available at Cancer Discovery Online (<http://cancerdiscovery.aacrjournals.org/>).

Received September 1, 2022; revised April 5, 2023; accepted May 30, 2023; published first June 1, 2023.

## REFERENCES

- Besic N, Vidergar-Kralj B, Frkovic-Grazio S, Movrin-Stanovnik T, Auersperg M. The role of radioactive iodine in the treatment of Hurthle cell carcinoma of the thyroid. *Thyroid* 2003;13:577-84.
- Maximo V, Sobrinho-Simoes M. Hurthle cell tumours of the thyroid: a review with emphasis on mitochondrial abnormalities with clinical relevance. *Virchows Arch* 2000;437:107-15.
- Lowe VJ, Mullan BP, Hay ID, McIver B, Kasperbauer JL. 18F-FDG PET of patients with Hurthle cell carcinoma. *J Nucl Med* 2003;44:1402-6.
- Gasparre G, Porcelli AM, Bonora E, Pennisi LF, Toller M, Iommarini L, et al. Disruptive mitochondrial DNA mutations in complex I subunits are markers of oncogenic phenotype in thyroid tumors. *Proc Natl Acad Sci U S A* 2007;104:9001-6.
- Corver WE, Ruano D, Weijers K, den Hartog WC, van Nieuwenhuizen MP, de Miranda N, et al. Genome haploidisation with chromosome 7 retention in oncogenic follicular thyroid carcinoma. *PLoS One* 2012;7:e38287.
- Tallini G, Hsueh A, Liu S, Garcia-Rostan G, Speicher MR, Ward DC. Frequent chromosomal DNA unbalance in thyroid oncogenic (Hurthle cell) neoplasms detected by comparative genomic hybridization. *Lab Invest* 1999;79:547-55.
- Mazzucchelli L, Burckhardt E, Hirsiger H, Kappeler A, Laissue JA. Interphase cytogenetics in oncogenic adenomas and carcinomas of the thyroid gland. *Hum Pathol* 2000;31:854-9.
- Maximo V, Soares P, Lima J, Cameselle-Teijeiro J, Sobrinho-Simoes M. Mitochondrial DNA somatic mutations (point mutations and large deletions) and mitochondrial DNA variants in human thyroid pathology: a study with emphasis on Hurthle cell tumors. *Am J Pathol* 2002;160:1857-65.
- Gopal RK, Kubler K, Calvo SE, Polak P, Livitz D, Rosebrock D, et al. Widespread chromosomal losses and mitochondrial DNA alterations as genetic drivers in Hurthle cell carcinoma. *Cancer Cell* 2018;34:242-55.
- Ganly I, Makarov V, Deraje S, Dong Y, Reznik E, Seshan V, et al. Integrated genomic analysis of Hurthle cell cancer reveals oncogenic drivers, recurrent mitochondrial mutations, and unique chromosomal landscapes. *Cancer Cell* 2018;34:256-70.
- Gopal RK, Calvo SE, Shih AR, Chaves FL, McGuone D, Mick E, et al. Early loss of mitochondrial complex I and rewiring of glutathione metabolism in renal oncocytoma. *Proc Natl Acad Sci U S A* 2018;115:E6283-E90.
- Simonnet H, Demont J, Pfeiffer K, Guenaneche L, Bouvier R, Brandt U, et al. Mitochondrial complex I is deficient in renal oncocytomas. *Carcinogenesis* 2003;24:1461-6.
- Mayr JA, Meierhofer D, Zimmermann F, Feichtinger R, Kogler C, Ratschek M, et al. Loss of complex I due to mitochondrial DNA mutations in renal oncocytoma. *Clin Cancer Res* 2008;14:2270-5.
- Ganly I, Ricarte Filho J, Eng S, Gosselin R, Morris LG, Liang Y, et al. Genomic dissection of Hurthle cell carcinoma reveals a unique class of thyroid malignancy. *J Clin Endocrinol Metab* 2013;98:E962-72.
- Dong Y, Gong Y, Kuo F, Makarov V, Reznik E, Nanjangud GJ, et al. Targeting the mTOR pathway in Hurthle cell carcinoma results in potent antitumor activity. *Mol Cancer Ther* 2022;21:382-94.
- Addie RD, Kostidis S, Corver WE, Oosting J, Aminzadeh-Gohari S, Feichtinger RG, et al. Metabolic reprogramming related to whole-chromosome instability in models for Hurthle cell carcinoma. *Sci Rep* 2020;10:9578.
- Ganly I, Liu EM, Kuo F, Makarov V, Dong Y, Park J, et al. Mitonuclear genotype remodels the metabolic and microenvironmental landscape of Hurthle cell carcinoma. *Sci Adv* 2022;8:eabn9699.
- Kobayashi M, Morishita H, Sugiyama N, Yokochi K, Nakano M, Wada Y, et al. Two cases of NADH-coenzyme Q reductase deficiency: relationship to MELAS syndrome. *J Pediatr* 1987;110:223-7.
- Pryma DA, Schoder H, Gonen M, Robbins RJ, Larson SM, Yeung HW. Diagnostic accuracy and prognostic value of 18F-FDG PET in Hurthle cell thyroid cancer patients. *J Nucl Med* 2006;47:1260-6.
- Morrison JA, Pike LA, Sams SB, Sharma V, Zhou Q, Severson JJ, et al. Thioredoxin interacting protein (TXNIP) is a novel tumor suppressor in thyroid cancer. *Mol Cancer* 2014;13:62.
- Parikh H, Carlsson E, Chutkow WA, Johansson LE, Storgaard H, Poulsen P, et al. TXNIP regulates peripheral glucose metabolism in humans. *PLoS Med* 2007;4:e158.
- Cancer Genome Atlas Research Network. Integrated genomic characterization of papillary thyroid carcinoma. *Cell* 2014;159:676-90.
- Rath S, Sharma R, Gupta R, Ast T, Chan C, Durham TJ, et al. MitoCarta3.0: an updated mitochondrial proteome now with sub-organelle localization and pathway annotations. *Nucleic Acids Res* 2021;49:D1541-D7.
- Mootha VK, Handschin C, Arlow D, Xie X, St Pierre J, Sihag S, et al. Erralpha and Gabpa/b specify PGC-1alpha-dependent oxidative phosphorylation gene expression that is altered in diabetic muscle. *Proc Natl Acad Sci U S A* 2004;101:6570-5.
- Yoo SK, Lee S, Kim SJ, Jee HG, Kim BA, Cho H, et al. Comprehensive analysis of the transcriptional and mutational landscape of follicular and papillary thyroid cancers. *PLoS Genet* 2016;12:e1006239.
- Subramanian A, Tamayo P, Mootha VK, Mukherjee S, Ebert BL, Gillette MA, et al. Gene set enrichment analysis: a knowledge-based approach for interpreting genome-wide expression profiles. *Proc Natl Acad Sci U S A* 2005;102:15545-50.
- Mootha VK, Lindgren CM, Eriksson KF, Subramanian A, Sihag S, Lehar J, et al. PGC-1alpha-responsive genes involved in oxidative phosphorylation are coordinately downregulated in human diabetes. *Nat Genet* 2003;34:267-73.
- Starck SR, Tsai JC, Chen K, Shodiya M, Wang L, Yahiro K, et al. Translation from the 5' untranslated region shapes the integrated stress response. *Science* 2016;351:aad3867.
- Kampinga HH, Hageman J, Vos MJ, Kubota H, Tanguay RM, Bruford EA, et al. Guidelines for the nomenclature of the human heat shock proteins. *Cell Stress Chaperones* 2009;14:105-11.
- Mick E, Titov DV, Skinner OS, Sharma R, Jourdain AA, Mootha VK. Distinct mitochondrial defects trigger the integrated stress response depending on the metabolic state of the cell. *Elife* 2020;9:e49178.
- Harding HP, Zhang Y, Zeng H, Novoa I, Lu PD, Calfon M, et al. An integrated stress response regulates amino acid metabolism and resistance to oxidative stress. *Mol Cell* 2003;11:619-33.
- Lehtonen JM, Forsstrom S, Bottani E, Viscomi C, Baris OR, Isoniemi H, et al. FGF21 is a biomarker for mitochondrial translation and mtDNA maintenance disorders. *Neurology* 2016;87:2290-9.

33. Khan NA, Nikkanen J, Yatsuga S, Jackson C, Wang L, Pradhan S, et al. mTORC1 regulates mitochondrial integrated stress response and mitochondrial myopathy progression. *Cell Metab* 2017;26:419–28.
34. Fiorese CJ, Schulz AM, Lin YF, Rosin N, Pellegrino MW, Haynes CM. The transcription factor ATF5 mediates a mammalian mitochondrial UPR. *Curr Biol* 2016;26:2037–43.
35. To TL, Cuadros AM, Shah H, Hung WHW, Li Y, Kim SH, et al. A compendium of genetic modifiers of mitochondrial dysfunction reveals intra-organellar buffering. *Cell* 2019;179:1222–38.
36. Kagan VE, Mao G, Qu F, Angeli JP, Doll S, Croix CS, et al. Oxidized arachidonic and adrenic PEs navigate cells to ferroptosis. *Nat Chem Biol* 2017;13:81–90.
37. Zou Y, Palte MJ, Deik AA, Li H, Eaton JK, Wang W, et al. A GPX4-dependent cancer cell state underlies the clear-cell morphology and confers sensitivity to ferroptosis. *Nat Commun* 2019;10:1617.
38. Dixon SJ, Patel DN, Welsch M, Skouta R, Lee ED, Hayano M, et al. Pharmacological inhibition of cystine-glutamate exchange induces endoplasmic reticulum stress and ferroptosis. *Elife* 2014;3:e02523.
39. Titov DV, Cracan V, Goodman RP, Peng J, Grabarek Z, Mootha VK. Complementation of mitochondrial electron transport chain by manipulation of the NAD<sup>+</sup>/NADH ratio. *Science* 2016;352:231–5.
40. Robinson BH, Petrova-Benedict R, Buncic JR, Wallace DC. Nonviability of cells with oxidative defects in galactose medium: a screening test for affected patient fibroblasts. *Biochem Med Metab Biol* 1992;48:122–6.
41. Doll S, Proneth B, Tyurina YY, Panzilius E, Kobayashi S, Ingold I, et al. ACSL4 dictates ferroptosis sensitivity by shaping cellular lipid composition. *Nat Chem Biol* 2017;13:91–8.
42. Soula M, Weber RA, Zilka O, Alvaseem H, La K, Yen F, et al. Metabolic determinants of cancer cell sensitivity to canonical ferroptosis inducers. *Nat Chem Biol* 2020;16:1351–60.
43. Yagi T, Seo BB, Nakamaru-Ogiso E, Marella M, Barber-Singh J, Yamashita T, et al. Possibility of transkingdom gene therapy for complex I diseases. *Biochim Biophys Acta* 2006;1757:708–14.
44. Hanahan D, Weinberg RA. Hallmarks of cancer: the next generation. *Cell* 2011;144:646–74.
45. Ju YS, Alexandrov LB, Gerstung M, Martincorena I, Nik-Zainal S, Ramakrishna M, et al. Origins and functional consequences of somatic mitochondrial DNA mutations in human cancer. *Elife* 2014;3:e02935.
46. Gorelick AN, Kim M, Chatila WK, La K, Hakimi AA, Berger MF, et al. Respiratory complex and tissue lineage drive recurrent mutations in tumour mtDNA. *Nat Metab* 2021;3:558–70.
47. Grandhi S, Bosworth C, Maddox W, Sensiba C, Akhavanfard S, Ni Y, et al. Heteroplasmic shifts in tumor mitochondrial genomes reveal tissue-specific signals of relaxed and positive selection. *Hum Mol Genet* 2017;26:2912–22.
48. Yuan Y, Ju YS, Kim Y, Li J, Wang Y, Yoon CJ, et al. Comprehensive molecular characterization of mitochondrial genomes in human cancers. *Nat Genet* 2020;52:342–52.
49. Molina JR, Sun Y, Protopopova M, Gera S, Bandi M, Bristow C, et al. An inhibitor of oxidative phosphorylation exploits cancer vulnerability. *Nat Med* 2018;24:1036–46.
50. Joshi S, Tolkunov D, Aviv H, Hakimi AA, Yao M, Hsieh JJ, et al. The genomic landscape of renal oncocytoma identifies a metabolic barrier to tumorigenesis. *Cell Rep* 2015;13:1895–908.
51. Thomas HE, Zhang Y, Stefely JA, Veiga SR, Thomas G, Kozma SC, et al. Mitochondrial complex I activity is required for maximal autophagy. *Cell Rep* 2018;24:2404–17.
52. Black JT, Judge D, Demers L, Gordon S. Ragged-red fibers: a biochemical and morphological study. *J Neurol Sci* 1975;26:479–88.
53. Arias-Mayenco I, Gonzalez-Rodriguez P, Torres-Torrel H, Gao L, Fernandez-Aguera MC, Bonilla-Henao V, et al. Acute O<sub>2</sub> sensing: role of coenzyme QH<sub>2</sub>/Q ratio and mitochondrial ROS compartmentalization. *Cell Metab* 2018;28:145–58.
54. Kang YP, Mockabee-Macias A, Jiang C, Falzone A, Prieto-Farigua N, Stone E, et al. Non-canonical glutamate-cysteine ligase activity protects against ferroptosis. *Cell Metab* 2021;33:174–89.
55. Zielke A, Tezelman S, Jossart GH, Wong M, Siperstein AE, Duh QY, et al. Establishment of a highly differentiated thyroid cancer cell line of Hurthle cell origin. *Thyroid* 1998;8:475–83.
56. King MP, Attardi G. Human cells lacking mtDNA: repopulation with exogenous mitochondria by complementation. *Science* 1989;246:500–3.
57. Arroyo JD, Jourdain AA, Calvo SE, Ballarano CA, Doench JG, Root DE, et al. A genome-wide CRISPR death screen identifies genes essential for oxidative phosphorylation. *Cell Metab* 2016;24:875–85.
58. Yang WS, Kim KJ, Gaschler MM, Patel M, Shchepinov MS, Stockwell BR. Peroxidation of polyunsaturated fatty acids by lipoxygenases drives ferroptosis. *Proc Natl Acad Sci U S A* 2016;113:E4966–75.
59. Viswanathan VS, Ryan MJ, Dhruv HD, Gill S, Eichhoff OM, Seashore-Ludlow B, et al. Dependency of a therapy-resistant state of cancer cells on a lipid peroxidase pathway. *Nature* 2017;547:453–7.
60. Ohye H, Sugawara M. Dual oxidase, hydrogen peroxide and thyroid diseases. *Exp Biol Med* 2010;235:424–33.
61. Bersuker K, Hendricks JM, Li Z, Magtanong L, Ford B, Tang PH, et al. The CoQ oxidoreductase FSP1 acts parallel to GPX4 to inhibit ferroptosis. *Nature* 2019;575:688–92.
62. Doll S, Freitas FP, Shah R, Aldrovandi M, da Silva MC, Ingold I, et al. FSP1 is a glutathione-independent ferroptosis suppressor. *Nature* 2019;575:693–8.
63. Mao C, Liu X, Zhang Y, Lei G, Yan Y, Lee H, et al. DHODH-mediated ferroptosis defence is a targetable vulnerability in cancer. *Nature* 2021;593:586–90.
64. Shaham O, Slate NG, Goldberger O, Xu Q, Ramanathan A, Souza AL, et al. A plasma signature of human mitochondrial disease revealed through metabolic profiling of spent media from cultured muscle cells. *Proc Natl Acad Sci U S A* 2010;107:1571–5.
65. Kremer DM, Nelson BS, Lin L, Yarosz EL, Halbrook CJ, Kerk SA, et al. GOT1 inhibition promotes pancreatic cancer cell death by ferroptosis. *Nat Commun* 2021;12:4860.
66. Dixon SJ, Lemberg KM, Lamprecht MR, Skouta R, Zaitsev EM, Gleason CE, et al. Ferroptosis: an iron-dependent form of nonapoptotic cell death. *Cell* 2012;149:1060–72.
67. Arai M, Imai H, Sumi D, Imanaka T, Takano T, Chiba N, et al. Import into mitochondria of phospholipid hydroperoxide glutathione peroxidase requires a leader sequence. *Biochem Biophys Res Commun* 1996;227:433–9.
68. Gaschler MM, Hu F, Feng H, Linkermann A, Min W, Stockwell BR. Determination of the subcellular localization and mechanism of action of ferrostatins in suppressing ferroptosis. *ACS Chem Biol* 2018;13:1013–20.
69. Gao M, Yi J, Zhu J, Minikes AM, Monian P, Thompson CB, et al. Role of mitochondria in ferroptosis. *Mol Cell* 2019;73:354–63.
70. Zhang W, Cui H, Wong LJ. Comprehensive one-step molecular analyses of mitochondrial genome by massively parallel sequencing. *Clin Chem* 2012;58:1322–31.
71. Davis CF, Ricketts CJ, Wang M, Yang L, Cherniack AD, Shen H, et al. The somatic genomic landscape of chromophobe renal cell carcinoma. *Cancer Cell* 2014;26:319–30.
72. Hicks SC, Okrah K, Paulson JN, Quackenbush J, Irazarry RA, Bravo HC. Smooth quantile normalization. *Biostatistics* 2018;19:185–98.
73. Love MI, Huber W, Anders S. Moderated estimation of fold change and dispersion for RNA-seq data with DESeq2. *Genome Biol* 2014;15:550.
74. Sharma R, Reinstadler B, Engelstad K, Skinner OS, Stackowitz E, Haller RG, et al. Circulating markers of NADH-reductive stress correlate with mitochondrial disease severity. *J Clin Invest* 2021;131:e136055.
75. Ritchie ME, Phipson B, Wu D, Hu Y, Law CW, Shi W, et al. limma powers differential expression analyses for RNA-sequencing and microarray studies. *Nucleic Acids Res* 2015;43:e47.
76. Zheng Z, Liebers M, Zhelyazkova B, Cao Y, Panditi D, Lynch KD, et al. Anchored multiplex PCR for targeted next-generation sequencing. *Nat Med* 2014;20:1479–84.
77. Doench JG, Fusi N, Sullender M, Hegde M, Vaimberg EW, Donovan KF, et al. Optimized sgRNA design to maximize activity and minimize off-target effects of CRISPR-Cas9. *Nat Biotechnol* 2016;34:184–91.